

# Simulation of hardened cement degradation and estimation of uncertainty in predicted failure times with peridynamics

**R.E. Jones**

*Sandia National Laboratories, Livermore, CA 94551*

**J.M. Rimsza**

*Sandia National Laboratories, Albuquerque, NM 87185*

**J.E. Trageser**

*Sandia National Laboratories, Albuquerque, NM 87185*

**J.R. Hogancamp**

*Sandia National Laboratories, Albuquerque, NM 87185*

---

---

*Preprint submitted to Construction and Building Materials*

*April 1, 2021*

# Simulation of hardened cement degradation and estimation of uncertainty in predicted failure times with peridynamics

**R.E. Jones**

*Sandia National Laboratories, Livermore, CA 94551*

**J.M. Rimsza**

*Sandia National Laboratories, Albuquerque, NM 87185*

**J.E. Trageser**

*Sandia National Laboratories, Albuquerque, NM 87185*

**J.R. Hogancamp**

*Sandia National Laboratories, Albuquerque, NM 87185*

---

## Abstract

Modeling the degradation of cement-based infrastructure due to aqueous environmental conditions continues to be a challenge. In order to develop a capability to predict concrete infrastructure failure due to chemical degradation, we created a chemomechanical model of the effects of long-term water exposure on cement [paste](#). The model couples the mechanical static equilibrium balance with reactive-diffusive transport and incorporates fracture and failure via peridynamics (a meshless simulation method). The model includes fundamental aspects of degradation of ordinary Portland cement (OPC) [paste](#), including the observed softening, reduced toughness, and shrinkage of the cement [paste](#), and increased reactivity and transport with water induced degradation. This version of the model focuses on the first stage of cement [paste](#) decalcification, the dissolution of portlandite. Given unknowns in the cement [paste](#) degradation process and the cost of uncertainty quantification (UQ), we adopt a minimally complex model in two dimensions (2D) in order to perform sensitivity analysis and UQ. We calibrate the model to existing experimental data using simulations of common tests such as flexure, compression and diffusion. Then we calculate the global sensitivity and uncertainty of predicted failure times based on variation of eleven unique and fundamental material properties. We observed particularly strong sensitivities to the diffusion coefficient, the reaction rate, and the shrinkage with degradation. Also, the predicted time of first fracture is highly corre-

lated with the time to total failure in compression, which implies fracture can indicate impending degradation induced failure; however, the distributions of the two events overlap so the lead time may be minimal. Extension of the model to include the multiple reactions that describe complete degradation, viscous relaxation, post-peak load mechanisms, and to three dimensions to explore the interactions of complex fracture patterns evoked by more realistic geometry is straightforward and ongoing.

*Keywords:* cement [paste](#), decalcification, portlandite, failure, fracture, chemical degradation, peridynamics.

---

## Highlights

- A chemomechanical model of degradation and fracture was developed for cement [paste](#) decalcification.
- The model was calibrated to experimental data and verified with multiple peridynamics simulations.
- Varying shrinkage qualitatively altered beam flexural response to degradation due to competing mechanisms.
- Uncertainty quantification and sensitivity provided a ranking of what mechanisms contribute to failure.

## 1. Introduction

The majority of infrastructure, including buildings, bridges, and dams, is constructed from ordinary Portland cement-based concrete which exhibits significant degradation as it ages [1, 2, 3]. While the bulk of existing research on the environmental attack of cement structures has focused on corrosion of embedded rebar [4, 5, 6], the cement [paste](#) itself can also degrade [7] and accelerate structural instability and failure. The mechanisms of cement [paste](#) degradation are complex due to the heterogeneous structure of the material [8] and can include sulfate attack, chloride attack, delayed ettringite formation, calcium leaching, pH sensitivities, alkali-aggregate reactivity, freeze-thaw cycles, excessive surface drying, and thermal cycles [9, 10, 11, 12, 13, 14]. This work focuses

on a specific aspect of cement [paste](#) degradation, decalcification, which occurs on time scales of  
20 months to years [15].

Ordinary Portland cement (OPC) [paste](#) is primarily calcium silicate hydrate (CSH,  $c\text{CaO} \cdot s\text{SiO}_2 \cdot w\text{H}_2\text{O}$ ), along with additional mineral phases including portlandite (CH,  $\text{Ca}(\text{OH})_2$ ), ettringite, and calcium trisilicate, among others [16, 14]. Water infiltration into cured, hydrated OPC leads to calcium leaching, and, after a sufficient length of time, CSH dissolution. Damage to the hardened  
25 cement [paste](#) that exposes fresh surface area, such as fracture, can accelerate localized decalcification and thereby facilitate additional mechanical degradation through weakening or removing constituents. Each of the mineral constituents that give hardened cement [paste](#) its strength react with water at varying rates, resulting in a series of reactions that overlap in time. Portlandite (CH) dissolution is the fastest reaction in OPC exposed to water, and its dissolution lowers the Ca to  
30 Si ratio (C/S). Generally, the C/S ratio in pristine OPC is at least 2.0, but OPC systems, such as concrete with aggregate, typically have slightly lower C/S ratios: 1.5–2.0 [17]. During the first stage of decalcification, CH dissolves from the OPC until the overall C/S ratio is about 1.4 [18]. This is followed by a slower second stage caused by gradual decalcification of the CSH phase and then a final stage with decalcification of the remaining high silicate phases [17]. While complete  
35 degradation of OPC requires years to decades, dissolution of CH from OPC in the first stage of decalcification, the focus of this work, occurs on the order of months to years [19, 20]. Additionally, the CH phase dissolves nearly completely, with only limited growth of ettringite following dissolution, in contrast to CSH which precipitates secondary phases and itself undergoes complex phase changes [21, 19]. The dissolution of CH degrades the mechanical properties of the OPC by  
40 increasing the porosity, reducing the elastic modulus of the material, and inducing local volumetric shrinkage [22, 23]. Increased porosity in the OPC increases the permeability, promoting more rapid water infiltration, diffusion and reaction. Decalcification of OPC causes shrinkage, due to  $\text{Ca}^{2+}$  removal from the CH and then the CSH structure [22]. On the other hand, when additional species are present in solution, such as  $\text{CO}_2$ ,  $\text{SO}_4^{2-}$ , or  $\text{Cl}^-$ , re-precipitation of secondary minerals, such as  
45 calcium carbonates, ettringite, and complex salts, can cause swelling and introduce additional local stresses [11, 13, 14]. It is critical to capture this first stage of decalcification, especially in concrete or cement systems that may have freshly exposed surface from fracture growth, in order to predict the stability of the system during aging.

Given the ubiquitous and technologically crucial applications of hardened cement paste (HCP)

50 and concrete, there are numerous experimental and simulation-based investigations of cement [paste](#) degradation. The water/cement ratio (W/C) [24, 25] and pH dependence on cement [paste](#) dissolution and fracture [26, 27] have been investigated experimentally. To achieve measurable degradation in laboratory scale experiments accelerants, such as ammonium nitrate, are often used to mimic slower dissolution reactions [28, 29, 30, 31, 32, 33]; however, some experiments with de-ionized [34] 55 and de-mineralized water [35] have been performed. The change in both porosity and C/S as a function of dissolved calcium ( $\text{Ca}^{2+}$ ) in ammonium nitrate is often reported [28, 29, 36, 37] as well as the near surface profiles, calcium content gradients [28, 29, 30] and other mineralogical changes in the leached zone [38, 39]. Decalcification fronts generally appear sharp, on the order of 1 mm [19, 20, 17], and, depending on the duration of immersion, the formation of multiple fronts have 60 also been observed [40].

Since cement decalcification occurs over years, well beyond the duration of typical experiments, models which simulate dissolution and degradation based on the physics and chemistry of the material are crucial for predicting outcomes. Given the historic, wide-spread use of OPC in structures, many models have been developed; however, since the material is complex, no single model covers 65 all the relevant phenomena. How the decalcification process affects the mechanical degradation is a primary focus of some modelling efforts. For instance, Le Bellégo *et al.* [41, 42, 43] and Pignatelli *et al.* [44] have developed models which rely on an empirical damage field, while Glasser *et al.* [24] employed a full reaction-diffusion chemical degradation model. Ulm *et al.* [45, 46, 47, 48] developed a chemoporoplasticity continuum framework to capture cement weakening during decalcification, which was connected to changes in the pore structure of the cement during degradation 70 [48]. Although not our topic of interest, there are many models of hydration, curing and concurrent shrinkage of cement [paste](#) [49]. The multiscale heterogeneity of concrete is another topic of interest. Stora *et al.* [50, 51] developed a numerical model based on a multi-scale homogenization approach to estimate the elastic and diffusive properties of cement materials during decalcification. 75 While this is not a comprehensive overview of the many OPC degradation models that have been developed, it highlights the varying approaches that have been taken to describe the dissolution of this complex material.

In this work, we develop a chemomechanical model employing the peridynamics framework [52, 53, 54] to describe HCP degradation and fracture focusing on the first stage of decalcification, 80 CH dissolution. Peridynamics (PD) is a meshless method of simulating a continuum material by

transforming the flux divergence of the typical conservation law into an integral evaluated with a particle-based quadrature. As an alternative to more traditional non-local simulation methods [55], it has some attractive qualities such as ease of implementation and parallel scaling. Furthermore, as a meshless method, peridynamics has an intrinsic ability to represent brittle fracture which makes this effort distinct from previously employed classical continuum methodologies such as finite elements [56, 57, 15] and related approaches that employ cohesive zones [5]. In related work peridynamics has been used to simulate chemical processes in metals such as pitting and stress-corrosion cracking in stainless steel [58, 59, 60, 61, 62] and has been extended to simulate crack growth from surface pitting [63]. Application of PD to cement or concrete systems has been largely focused on fracture and phenomenological models of damage. For instance, Demmie *et al.* [64] modelled large-scale impact of concrete, and Huang *et al.* [65] also employ PD to simulate dynamic failure of concrete. Gerstle *et al.* [66] employed quasi-static PD solutions to demonstrate that the simple tensile damage model of traditional PD can replicate fracture observed in concrete structures. More broadly, Das *et al.* [67] simulated flexural tests in mortar, Jing *et al.* [68] simulated nanoindentation of CSH, and Yaghoobi *et al.* [69, 70] modelled fracture of cementitious composites with PD. Also notable is work on the apparent mesoscales introduced by concrete formed from cement matrix aggregates. Yang *et al.* [71] developed a model of corroding rebar in a cement matrix. Li *et al.* [72] modelled a cement matrix with hard aggregates and interface zones with PD. Hou *et al.* [73] explored effects of W/C and curing on the overall mechanical response by systematically adjusting the mechanical properties of the aggregate. In related work Zhao *et al.* [6] used a multiscale PD framework to model the swelling due to the corrosion of rebar embedded in concrete. Very little of the previous PD-based efforts on cement materials includes the role of environmental conditions on the material properties of the system. Most work that includes water as a factor in fracture focuses on pressure driven fracture growth [74, 75, 76, 77, 78] rather than modeling the weakening of the material due environmental conditions. Closest to our present effort, Li *et al.* [79] developed coupling of mechanical and diffusive transport via PD to simulate chloride penetration [80]. In a quasi-static mechanical and dynamic transport regime, their model changed the diffusivity of the material based on local critical damage and critical bond stretch. Unlike our developments it appears that transport and reaction effects on mechanics, such as shrinkage, were not modelled. As with most previous work with PD, we do not model full poroelasticity effects, viscoplasticity and finite-size effects [81, 82] and leave this phenomenology for future work.

Given unknowns in the HCP degradation process and the cost of uncertainty quantification (UQ), we adopt a minimally complex model in two dimensions (2D) in order to perform global sensitivity analysis and UQ after validating and calibrating the model with experimentally measured properties. With this model we provide insight into the most sensitive inputs and variance in the outcomes of the degradation process. Given the large number of physical properties (11) this is still a considerable task that is complicated by the fact that the PD model parameters are indirectly associated with measured properties. In addition to providing a relatively simple and complete chemomechanical model of HCP degradation with an investigation of the influence of material properties on failure, we also present an number of methodological innovations for peridynamics: (a) tuning of the integration scheme to obtain low order accuracy, (b) a scheme for regularizing failure in a quasistatic deformation mode, (c) penalty based boundary conditions that emulate tradition pin and roller supports, and (d) dynamic boundary conditions to effect fluid influx into fractured regions.

In the next section (Sec.2) we describe the phenomenology of HCP degradation. We focus on and develop a chemomechanical framework to model the interaction of mechanics and reactive-diffusive chemical transport. In contrast to micromechanical models, we take a phenomenological approach for simplicity and parsimony of the parameters that need to be calibrated. Examining the available experimental data we reduce chemical reaction and species transport to a phenomenological model involving minimum number of transporting and reacting species. Reaction and diffusion of crucial species are included, as are coupled chemomechanical effects such as shrinkage and porosity induced diffusivity changes and fracture induced infiltration. In Sec.3 we describe the PD-based numerical methods we employ to simulate the phenomenology described in Sec.2 with full details given in the Appendix. With the proposed model and newly developed methods we produce the results described in Sec.4. This section begins with the procedure we used to calibrate the phenomenological model to experimentally measured properties. Since the available experimental data treats individual aspects of the range of phenomenology we want to capture, we calibrate to particular properties in sequence starting with the mechanical properties and then adding calibration to the transport and chemical properties. We use a sequence of simulations of common experimental tests (three point beam bending, beam compression, static cylinder shrinkage, point source diffusion and diffusion front propagation) to (a) determine the model parameters, and (b) ensure that the model behavior conforms to expectations by comparison with analytical solutions and published experiments. With

the calibrated model we validate the overall chemomechanical response with a beam in three point bending subject to chemical attack. With this in hand, we explore the effects of uncertainty in the physical properties have on predictions of long term behavior. We conclude with a discussion of the ramifications of the results, and a summary of the innovations and limitations of the model in Sec. 5.

## 2. Phenomenology

Our goal is to model the decalcification behavior of cement based materials. In this work we focus on hardened cement paste (HCP) in the presence of water. In this section we outline both the governing equations and the constitutive behavior before providing an exposition of the method and model in Sec. 3 and the Appendix. Fundamentally, HCP is a brittle elastic material which fractures readily in tension and has limited compressive strength. As mentioned in the Introduction, in the presence of water HCP degrades through preferential leaching of certain chemical species. Traditionally water infiltrated HCP has been modelled with poroelasticity [48] and related theories [43, 24, 44]. Here we developed a PD based fluid-solid coupled mixture model. The phenomenological effects of chemically-induced mechanical degradation [46] of HCP included in the model are: (1) softening: decrease of elastic modulus, (2) weakening: decrease of fracture toughness, (3) swelling: increase of stress-free reference volume, (4) increased permeability/diffusivity of water, and (5) increased cement-water reactivity. Given the complexity of HCP, all the measured properties have variability, which we have attempted to quantify in Table 1 given the existing literature and demonstrate their effects on structural outcomes in the UQ analysis in Sec. 4.3.

### 2.1. Governing equations

Degradation of HCP is an example of the coupled physics of chemomechanics. Since HCP degradation is a slow process, the quasistatic local mechanical balance of linear momentum

$$\mathbf{0} = \nabla_{\mathbf{x}} \cdot \mathbf{P} + \rho \mathbf{b} \quad (1)$$

governs the displacement  $\mathbf{u}$  of the solid, where  $\mathbf{P}$  is the first Piola-Kirchhoff stress,  $\rho$  is the (reference) mass density, and  $\mathbf{b}$  is a body force such as gravity. In a Lagrangian description, the displacement  $\mathbf{u}(\mathbf{X}, t) = \mathbf{x}(\mathbf{X}, t) - \mathbf{X}$  is a function of reference position  $\mathbf{X}$  and time  $t$ , where  $\mathbf{x}$  is the current



Property		Pristine value	range	Degraded range	References
Young's modulus [GPa]	$E$	30	23-34	3-16	[83, 84, 50, 21]
Poisson's ratio*	$\nu$	0.25	0.25-0.28	–	[83, 85]
Fracture toughness [MPa-cm <sup>1/2</sup> ]	$K_{Ic}$	2.8	2.5-3.0	1.8-2.3	[86, 87, 88]
Compressive strength [MPa]	$\sigma_c$	35	30-41	21-33	[89, 90, 91, 92, 28]
Diffusivity [cm <sup>2</sup> /yr]	$D$	1.4	0.026-3.7	5.8-28.5	[17, 93, 20, 94, 95, 56]
Reaction rate† [1/yr]	$K$	<i>22</i>	<i>18-33</i>	<i>47-66</i>	[96, 97, 20]
Volumetric shrinkage	$\vartheta$	0.0	0.0	0.0056–0.0066	[98, 22, 23]
Porosity	$\phi$	0.25	0.14–0.40	0.38–0.80	[99, 47, 93, 100, 20, 31]

Table 1: Nominal values and ranges of material properties for cement paste with water/cement ratio (W/C) 0.4–0.5 and aged 28 days. Directly measured values are in roman font, and derived values are in italics (see Sec. 2.5). Note Poisson's ratio\* is fixed at 0.25 by the numerical formulation, and change in reaction rate† is estimated by the change of surface area via the change of porosity using a fixed decalcification rate per surface area.

position of  $\mathbf{X}$ . The mechanical process is coupled to reactive transport of the chemical species governed by

$$\dot{c} = \nabla_{\mathbf{x}} \cdot \mathbf{j} + r \quad (2)$$

where  $c = c(\mathbf{x}, t)$  is a list of relevant species concentrations,  $\mathbf{j}$  is the concentration flux, and  $r$  is a net species generation list due to chemical reactions. The dependent fields of these balance equations,  $\mathbf{u}$  and  $c$ , are coupled through constitutive equations of fluxes  $\mathbf{P}$  and  $\mathbf{j}$ , and the source  $r$ .

## 2.2. Mechanics

Cement [paste](#) is a brittle material, hence small strain elasticity with the possibility of fracture is an appropriate constitutive theory. (Cement [paste](#) also displays poroplastic [46] and viscous behavior [101] but this is beyond the scope of this work.) In isotropic linear (small-strain) elasticity the stress  $\mathbf{P}$  is given by:

$$\mathbf{P} = E \left( \frac{\nu}{(1+\nu)(1-2\nu)} (\mathbf{I} \cdot \boldsymbol{\epsilon}) \mathbf{I} + \frac{1}{1+\nu} \boldsymbol{\epsilon} \right) \quad (3)$$

where the strain is  $\boldsymbol{\epsilon} = \frac{1}{2} (\nabla \mathbf{u} + \nabla^T \mathbf{u})$  and the elastic moduli are expressed in terms of two independent constants, *e.g.* Young's modulus  $E$  and Poisson's ratio  $\nu$ . For two-dimensional (2D)

170 plane strain,  $\mathbf{I}$  is the 2D identity tensor and  $\boldsymbol{\epsilon}$  and  $\mathbf{P}$  are likewise specialized to their in-plane components.

We treat shrinkage/swelling of HCP like growth/phase change, *i.e.* via volumetric change of reference configuration [46].

$$\mathbf{P} = \mathbf{P}(\boldsymbol{\epsilon}) + B\vartheta \mathbf{I} \quad (4)$$

where  $\vartheta$  is the volumetric dilation strain due to shrinkage which can be related to a radial strain  $\alpha$  via  $\vartheta = (1 + \alpha)^3 - 1 \approx 3\alpha$ . For 2D plane strain, the bulk modulus  $B$  is

$$B = \frac{E}{(1 + \nu)(1 - 2\nu)} \quad (5)$$

This formulation is essentially identical to elasticity with thermal expansion (or a chemistry induced pore pressure [102]). The correlated effects of degradation, such as elastic softening and loss of fracture toughness [103], will be discussed in Sec. 2.5. Fracture is handled intrinsically by PD as  
 175 an extension of elasticity, which will be discussed in Sec. 3, as will the mechanism to allow for fluid infiltration to accompany fracture.

### 2.3. Chemistry

The chemical aspects of degradation involve both species transport and localized reactions. In the leaching process, calcium bound in the CH in the cement paste is dissolved in the presence of water. As discussed in the Introduction, three reactions are important in the degradation of HCP [104]. We focus on the early (1–10 year) time-frame, where dissolution of CH ( $\text{Ca}(\text{OH})_2$ ) dominates:



Here, the underline denotes a solid bound species to distinguish it from mobile species. Chemical theory suggests that the reaction rate  $r$  is dependent on the local concentrations of reactants and products and the exposed surface area of the porous HCP. A standard model of the net forward rate of the reaction (6) is

$$r = r(c_{\underline{\text{Ca}(\text{OH})_2}}, c_{\text{Ca}^{2+}}, c_{\text{OH}^-}) \approx K_{\text{fwd}} c_{\underline{\text{Ca}(\text{OH})_2}} - K_{\text{rev}} c_{\text{Ca}^{2+}} c_{\text{OH}^-}^2 , \quad (7)$$

where  $K_{\text{fwd}}$  and  $K_{\text{rev}}$  are reaction rate parameters which depend on the exposed surface area per volume  $\varsigma$ . Here, the effects of pH on the reaction rate due to the concentration  $c_{\text{OH}^-}$  of  $\text{OH}^-$  is  
 180 apparent.

Implicit in reaction (6) and Eq. (7) is the presence of water. Generally, the pores in hydrated, cured cement [paste](#) are at least partially saturated [105, 106, 107, 108, 109, 110] with fluid. If the pore solution is assumed to be in (chemical) equilibrium  $r = 0$ , the ratio of equilibrium concentrations [104]

$$\frac{c_{\text{Ca}^{2+}}}{c_{\text{Ca}(\text{OH})_2}} c_{\text{OH}^-}^2 = \frac{K_{\text{fwd}}}{K_{\text{rev}}} \quad (8)$$

determines the relative magnitudes of the forward and the reverse reaction rate coefficients. This appears to be a means of obtaining  $K_{\text{fwd}}$  and  $K_{\text{rev}}$  from measured net forward reaction rates and equilibrium concentrations; however,  $\text{Ca}(\text{OH})_2$ , being a solid bound species only exposed at surface, does not have a well-defined volumetric concentration.

We assume that the HCP with partially saturated pores is sufficiently permeable that dissolved species are mobile and transport via concentration driven diffusion [111, 36, 80, 57, 79]. For our applications, where the HCP is exposed to environmental water there is an efflux of dissolved  $\text{Ca}^{2+}$  through diffusion thereby disturbing the equilibrium in the pores and allowing the CH dissolution (6) to proceed,  $r \gg 0$ . The specific form of Eq. (2) for this process:

$$\begin{aligned} \dot{c}_{\text{Ca}^{2+}} &= \nabla \cdot (D_{\text{Ca}^{2+}} \nabla c_{\text{Ca}^{2+}}) + r \\ \dot{c}_{\text{OH}^-} &= \nabla \cdot (D_{\text{OH}^-} \nabla c_{\text{OH}^-}) + 2r \\ \dot{c}_{\text{Ca}(\text{OH})_2} &= -r \end{aligned} \quad (9)$$

185 introduces the effective diffusion coefficients  $D_{\text{Ca}^{2+}}$  and  $D_{\text{OH}^-}$  for the mobile species which account for permeability and tortuosity of the porous HCP [111]. The coefficients of  $r$  in Eq. (9) are given by stoichiometry.

To illustrate a fundamental aspect of this model, we assume that  $\text{Ca}^{2+}$  is the crucial species in this reaction and reduce Eq. (7) by assuming fixed pH ( $c_{\text{OH}^-}$ ). Preliminary simulations with  
190 this assumption, see Fig. 1, show that: (a) the dissolved calcium remains in (quasi-)equilibrium with the bound calcium, and (b) the reaction front is diffuse (spanning tens of cm). These results are similar for an effective  $\text{Ca}^{2+}$  diffusion constant  $D_{\text{Ca}^{2+}}$  in HCP in range  $10^{-12}$  to  $10^{-11}$  m<sup>2</sup>/s [111, 98, 49, 12, 112, 57], *i.e.* the reaction is fast compared to the diffusion and therefore is diffusion limited. The diffuse front is manifestly incompatible with experiments that we are trying to model  
195 [19, 20, 17] where the front is confined to a width of order  $\ll 1$  cm. This simulation and the fact that  $\frac{c_{\text{Ca}^{2+}}}{c_{\text{Ca}(\text{OH})_2}}$  remains nearly constant in some experiments [104] suggest that changing the pH of

the pore solution with the influx of environmental water may be the determining factor [26, 27]. (For reference the C/S to  $c_{\text{Ca}^{2+}}$  ratio is  $\approx 0.73$  mmol/L at  $w/c=0.6$  over the C/S range of interest [1.4, 2.5] [104].) Nevertheless the diffuse front is a signature of models of the type Eq. (9).

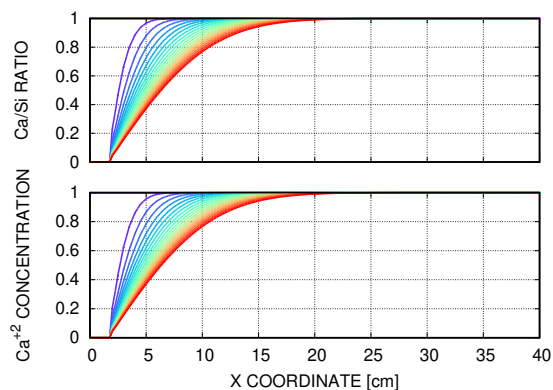


Figure 1: Reaction diffusion model of dissolved  $\text{Ca}^{2+}$ . Concentrations have been normalized so that: (a)  $\text{Ca}^{2+}$  in pores in initial equilibrium is 1 and in environmental water is 0, (b) calcium to silica ratio is 1 initially and 0 fully degraded. Left boundary is in contact with environmental water, right boundary is impermeable. Sequence over 100 years (blue: 5 years, red:100 years)

#### 200 2.4. Simplified reaction-diffusion model

Instead of using the reaction-diffusion model Eq. (7) directly, we take a more empirical approach to simulate the essential phenomenology of the decalcification front and the attendant mechanical changes. Two aspects of Eq.(7) are crucial to the phenomenology we are interested in (a) the transport of mobile species that initiates the reaction and (b) the bound Ca that (in large part) determines the state of the solid HCP. Since contact of HCP with environmental water changes the pH in the pores and encourages transport of dissolved  $\text{Ca}^{2+}$ , we lump all the mobile species together and model their transport with

$$\dot{\tilde{c}} = \nabla \cdot (D \nabla \tilde{c}) . \quad (10)$$

based on the available effective diffusion constants for water in HCP [17, 93, 20, 94, 95, 56]. Here,  $\tilde{c}$  is a non-dimensional concentration tracking the efflux of dissolved species and the corresponding influx of purer water ( $\tilde{c} = 0$  in undisturbed pores and  $\tilde{c} = 1$  in environmental water). Regarding the solid species, in experiments the state of the solid is usually described in terms of: (a) the C/S

ratio, for which we would need equations and reactions to track the silicon, or (b) the dissolved calcium concentration, which is easier to measure but is only an indirect indicator of the state of the solid in a closed experimental system. In the following, we take  $\underline{c}$  to be a non-dimensional solid state / degradation variable correlated with the C/S ratio, such that  $\underline{c} = 1$  in pristine HCP (C/S  $\approx 2.5$ ) and  $\underline{c} = 0$  in fully degraded HCP (C/S  $\approx 1.0$ – $1.5$ ) [113, 42]. Its evolution is governed by

$$\dot{\underline{c}} = r(\tilde{c}, \underline{c}) = -\hat{K}(\tilde{c}, \underline{c}) \underline{c} \quad (11)$$

where the function  $\hat{K}(\tilde{c}, \underline{c})$  is monotonic with  $\tilde{c}$  and its dependence on  $\underline{c}$  is to effect degradation which will be discussed in the next section.

There is limited data for the effective rate constant  $\hat{K}$ . Bullard *et al.* [97] report a dissociation rate constant  $k_d = 7.2 \mu\text{mol}/(\text{m}^2\text{s})$  corresponding to the forward reaction Eq. (6) in fully immersed conditions, which is in terms of moles of  $\text{Ca}(\text{OH})_2$  dissolved per exposed surface area  $A$  of the concrete paste. We make this value consistent with Eq. (11) by transforming it to a volumetric basis. We multiply it by the specific surface area of concrete  $\varsigma = A/V$ , and then normalize by the initial molar concentration  $c_p = f\rho/\eta$  of the  $\text{Ca}(\text{OH})_2$  to obtain:

$$\hat{K}(1, 1) = \frac{\varsigma}{c_p} k_d \approx 0.04 \in [0.03, 0.06] 1/s \quad (12)$$

where  $f \in [0.20, 0.25]$  is the volume fraction of  $\text{Ca}(\text{OH})_2$  in cement paste [34],  $\eta = 74.09 \text{ g/mol}$  is the molar mass of  $\text{Ca}(\text{OH})_2$ ,  $\rho = 2.23 \text{ g/cm}^3$  is the mass density of  $\text{Ca}(\text{OH})_2$  [114, 115, 116].

205 We approximate the specific volume  $\varsigma \in [33, 50] \text{ 1}/\mu\text{m}$  with Eq. (20) in the next section given the available data.

This reduced reaction-diffusion model allows forward reactions only in the presence of a diffusion driven front. It omits re-binding/precipitation of CH and significant build up of reaction products since the dissolution reaction tends to be strongly biased to the forward reaction [15, 117]. More  
210 details of the form of  $\hat{K}$  will be given in Sec. A.2. Overall, these simplifications limit the number of parameters for calibration and UQ, and the simplicity of the model aids in interpretation of predictions.

## 2.5. Chemo-mechanical degradation and coupling

Now that we have a variable,  $\underline{c}$ , that determines the state of HCP and an equation for its evolution, Eq. (11), we can use it to model the effects of chemical degradation on related mechanical

and transport processes. Given the variety and level of detail of available data, we employ a linear model with “pristine” ( $\underline{c} = 1$ ) and “degraded” ( $\underline{c} = 0$ ) endpoints of the state variable  $\underline{c} \in [0, 1]$  of the solid. For example, for the elastic stiffness

$$E = E_1 + \underbrace{(E_0 - E_1)}_{\Delta E} (1 - \underline{c}) , \quad (13)$$

where  $E_1$  is the pristine value of Young’s modulus and  $E_0$  is the degraded value. The change in elastic modulus is roughly proportional to the change in porosity of the HCP, refer to Table 1, as we would expect for simple mixture behavior. Also the exponential decay of stiffness shown in Nguyen *et al.* [118] Fig. 13 is consistent with Eq. (13) given diffusion and first order reaction kinetics. We employ a linear model of this type for each parameter in Table 1:

$$\text{Young's modulus} \quad E = \bar{E} + \Delta E \quad (1 - \underline{c}) \quad (14)$$

$$\text{Fracture toughness} \quad K_{\text{Ic}} = \bar{K}_{\text{Ic}} + \Delta K_{\text{Ic}} (1 - \underline{c}) \quad (15)$$

$$\text{Compressive strength} \quad \sigma_c = \bar{\sigma}_c + \Delta \sigma_c \quad (1 - \underline{c}) \quad (16)$$

$$\text{Volumetric stretch} \quad \vartheta = 1 + \Delta \vartheta \quad (1 - \underline{c}) \quad (17)$$

$$\text{Diffusivity} \quad D = \bar{D} + \Delta D \quad (1 - \underline{c}) \quad (18)$$

$$\text{Reaction rate} \quad K = \bar{K} + \Delta K \quad (1 - \underline{c}) \quad (19)$$

with one exception: we assume that the HCP’s Poisson’s ratio does not change with degradation.

215 This formulation, given the measured values in Table 1, leads to a less stiff, less tough mechanical response as the bound Ca is removed by the dissolution reaction  $\underline{c} \rightarrow 0$ . This approach has been used before, for instance in Ref. [28], and is supported by experimental findings [50, 21]. Further corroborating this approach, the correlated effects of elastic softening and decrease in fracture toughness, for instance, have been measured [41, 103] and modelled [41, 119, 44] for Ca leaching  
220 and the related alkali-silica degradation mechanism.

Since both degradation-induced porosity and fracture can change the transport of water and reactivity in the HCP, we treat these two effects separately. Changes in diffusivity due to changes in porosity are handled implicitly using the pristine-degraded linear model Eq. (13) for  $D$ , as opposed to the more traditional route of tying these changes directly to porosity [34]. Fracture induced  
225 infiltration is modelled with dynamic boundary conditions based on local bond breakage/damage which will be described in Sec. A.3. For our applications, we assume changes in (volumetric)

reactivity are primarily influenced by surface area [120] so that  $\hat{K} \propto \varsigma$  and the specific dissolution rate constant  $k_d$  is constant.

For the proposed model we are only concerned with relating change in porosity to changes in surface area and therefore reactivity. (The details of the porosity distribution do not influence the model). To capture first order pore surface-volume effects, we reduce the void size distribution to the single statistic: average pore radius  $\bar{r}$ , which has been measured to be in the range 10–15 nm [121, 99] for HCP. Given limited available information, we relate the changes in  $\hat{K}$  to changes in  $\phi$  given in Table 1 holding the range of  $\bar{r}$  fixed. Specifically, we assume spherical voids with average radius  $\bar{r}$  and known porosity  $\phi$ , so that the reaction coefficient  $\hat{K}$  can be estimated by:

$$\hat{K} \propto \varsigma \approx \frac{n\bar{a}}{V} = \frac{3\phi}{\bar{r}} \propto \phi . \quad (20)$$

*i.e.* a proportionality to porosity with the coefficient of proportionality determined by the nominal values of  $K$  and  $\phi$ . This simple model is supported by the experiments of Thomas *et al.* [122] which show that surface area of HCP increases as C/S goes from  $\approx 3$  to  $\approx 1$ . (A more detailed model, such as integrating a population of spherical voids over the nearly Gaussian distribution of sizes shown in Halperin *et al.* [99] or approximating the complex distributions in Haga *et al.* [19, 20], is not warranted given the level of approximation in the overall model.)

### 3. Method

We employ peridynamics (PD) to perform full field, boundary value simulations with the model described in the previous section. Peridynamics [52] is a regularization of standard local continuum balance laws, such as Eq. (1), that uses computational particles and spatially compact kernels in its formulation. The full theory is described and developed in the work of Silling *et al.* [53, 54]. Briefly, smooth kernels connect computational particles to continuous physical fields. The kernels have compact support within a ball  $B_h$  with radius  $h$  also known as the *horizon*. They serve two functions: (a) to localize and smooth the point data, and (b) to transform the kinematic point data to kinetic fields. Localization can be achieved with a variety of kernels, *e.g.* uniform/top hat or bell-shaped functions. The horizon relative to the point spacing must be large enough for sufficient accuracy in the integration of the kernel via an unstructured point-based, low-order quadrature, see further discussion in Sec. A.1.

For concrete structures, the characteristic size of domain  $L$  is on the order of 0.1–100 m. For brittle fracture, the characteristic flaw size is typically 1 nm to 1 mm. For the water diffusion, the diffusion depth is  $\propto \sqrt{Dt}$  where  $t$  is 1–10 years and the depth is 10–100 mm, based on values in Table 1. These physical scales puts constraints on the spatial resolution  $s$ .

Constitutive models are needed for the physical response, in our case mechanical stress (momentum flux) and diffusion/concentration flux. For this work we adopt the simpler bond-based formulation of PD [71] which, like central force potentials, restricts the mechanical response to Navier elasticity with a fixed Poisson’s ratio of  $\nu = 1/4$ . Conveniently, HCP has a Poisson’s ratio of  $\approx 0.25$ , refer to Table 1. The Appendix gives the details of our implementation of the proposed model with the peridynamics (PD) method and specific enhancements needed to model coupled chemo-mechanical fracture. Most salient to the results is the translation of the mechanical and chemical properties listed in Table 1 to the PD parameters: the bond stiffness,  $k$ , directly related to the elastic moduli; the minimum and maximum bond stretches,  $\lambda_{\min}$  and  $\lambda_{\max}$ , that control fracture toughness and compressive strength; the equilibrium bond stretch,  $\alpha$ , which effects shrinkage or swelling; the bond diffusivity,  $\kappa$ , which is directly related to chemical diffusivity. The nominal values of these parameters are calibrated to the measured physical properties using physical tests and experimental data in the next section. Scaling relations described in the Appendix provide the means to obtain the PD parameters associated with degraded and uncertain properties. In addition to adapting the PD model to volumetric changes (shrinkage, swelling or phase changes), we also developed dynamic boundary conditions to simulate fluid infiltration into fractures. The Appendix gives an exposition of the pin and roller boundary conditions we developed to emulate loading in three point bending and similar tests. The Appendix also gives other methodological details such as the horizon tuning we employ for optimal accuracy.

## 4. Results

To make predictions of HCP failure, we first calibrate the PD model to the nominal properties in Table 1 using a variety of model problems described in Sec. 4.1. The calibrated nominal model parameters are summarized in Table 2, as are the scaling relationships with the measured material properties. The nominal calibrated values of the PD parameters in Table 2 determine the scaling coefficients, and thus all other parameter values can be obtained from the pristine and degraded physical properties and their ranges in Table 1.



Parameter	Value	Scaling
Horizon* [cm]	0.89	$h = 1.78 s$
Stiffness [GPa/cm]	13	$k = 3.8 \frac{E}{h}$
Tensile critical stretch	$7.74 \times 10^{-5}$	$\lambda_{\max} = 0.78 \frac{K_{Ic}}{E\sqrt{h}}$
Compressive critical stretch	$-2.27 \times 10^{-3}$	$\lambda_{\min} = -2.5 \frac{\sigma_c}{E}$
Diffusivity [1/cm-yr]	8.2	$\kappa = 5.2 \frac{D}{h}$
Reactivity [1/yr]	-22	$K \equiv K$
Shrinkage	-0.002	$\alpha \approx 3\vartheta$

Table 2: Calibrated nominal PD model parameters and property-to-parameter scaling maps for  $s = 0.50$  cm,  $h = 0.89$  cm. \*Note the horizon  $h$  was calibrated based on quadrature error.

After calibration, we explore the phenomenology of the coupled chemomechanical system with a beam in bending subject to chemical attack. Then with a representation of the buckling of a beam due to water infiltration, we explore the sensitivities of the failure outcomes to the pristine and de-  
280 graded material properties and their uncertainties. In order to make the uncertainty quantification (UQ) studies feasible with the available computational resources, we needed to balance the domain size  $L$  and field resolution  $s$ . Using the diffusion coefficient in Table 1 we estimate that the water diffusion front progresses about 1 cm in undamaged HCP in 1 year, about 3 cm in 10 years, and about 11 cm in 100 years. So we target structures where the characteristic length  $L$  is on the order  
285 of 10-100 cm. The reaction-diffusion front width is about 0.25 cm based on  $\sqrt{\frac{D}{K}}$ , which gives a scale for the resolution; however, the finest fracture scales are unresolvable.

#### 4.1. Calibration

Peridynamic parameters are not usually measured directly, unlike material properties such as Young's modulus  $E$  of a solid and the diffusion coefficient  $D$  of a mobile/dissolved species. Ana-  
290 lytic expressions that relate the PD parameters to the material properties, such as Eq. (A.41) and Eq. (A.42), are limited in that they are only tuned to part of the response, *e.g.* volumetric deformation. Furthermore they generally depend strongly on the horizon  $h$  (refer to Table 2 and the

Appendix). For each PD property we employ a calibration problem where the continuum solution is known, at least semi-analytically, to obtain the nominal parameters and the scaling coefficients in Table 2 from the nominal measured properties in Table 1.

#### 4.1.1. Mechanical

To calibrate the PD stiffness parameter  $k$  and critical stretch  $\lambda_{\max}$  we employ a three point beam bending test, see schematic in Fig. 2. The height of the rectangular beam  $H$  is 10 cm, the length  $L$  is 80 cm, and the supports are separated by  $l = 64$  cm. The point supports are modeled with horizontal roller boundary conditions applied to 1 cm radius semi-disk penalty regions (see Sec. A.3) centered at the surface of the beam; likewise, the point force is effected with a pin constraint on a 1 cm semi-disk penalty region and the reaction force on the same region is recovered via Eq. (A.36).

We used an un-notched ( $a=0$ ) beam to connect Young's modulus  $E$  to the bond stiffness  $k$  through the beam's flexural modulus. The linear elastic approximate analytical solution for  $U$  the displacement of the center support is

$$U = \frac{1}{4E} \frac{l^3}{H^3} F \quad (21)$$

where  $l$  is the length between supports,  $H$  is the beam height, and  $F$  is the force per out-of-plane beam thickness. Note there is no dependence on Poisson's ratio and the solution is linear in thickness. A beam with a pre-existing slit notch of length  $a$  provides a connection with fracture toughness  $K_{Ic}$  [123] through the semi-analytical relation:

$$K_I = \frac{f(a/H)}{\sqrt{H}} \frac{l}{H} F_{\text{peak}} \quad (22)$$

where

$$f(x) = \frac{3\sqrt{x}}{2(1+2x)(1-x)^{3/2}} (1.99 - x(1-x)(2.15 - 3.93x + 2.7x^2)) .$$

Fig. 3 compares the PD simulated response, with calibrated  $k$  and  $\lambda_{\max}$ , to the analytic continuum solutions Eq. (21) and (22) for a sequence of node spacings  $s$  and tuned horizons  $h$  (from Table 4). For each run, the slit height  $a$  was 1 cm, and the slit width is less than the node spacing  $s$ . The elastic region conforms to expectations of a linear force-displacement curve with the slope determined by the bending modulus Eq. (21). Furthermore the post elastic trend is characteristic of beam bending experiments on HCP and related materials [41, 43, 44] which display a gradual softening to peak load and then a rapid decay sometimes followed by a more gradual decline. The correspondence of the PD simulation with the post-peak response shown in Ref. [41], for instance,

is qualitative. In fact, the data on mortar beams shows non-ideally brittle behavior which requires more complex PD bond functions to model the long tails of the force-displacement curves (see further discussion in the Conclusion).

The run times for various resolutions were:  $s=1\text{cm}$ : 3 CPU-minutes,  $s=0.5\text{ cm}$ : 29 CPU-  
 315 minutes,  $s=0.33\text{ cm}$ : CPU-155 minutes,  $s=0.25\text{ cm}$ : 462 CPU-minutes. Given the accuracy versus  
 expense trade-off and the need for  $\approx 10^4$  simulations for the UQ studies, we chose  $s=0.5\text{cm}$  with  
 $h=1.7841s$  for the subsequent simulations. For this choice we verified the tuned  $k$  gives an elastic  
 response consistent with Young's modulus  $E$  using independent tension simulation (dimensions  
 $4\text{cm}\times 8\text{cm}$ ) with minimal roller boundary conditions to allow for Poisson effects and maintain a  
 320 (nearly) homogeneous stress state.

With  $k$  and  $\lambda_{\max}$  calibrated, we then calibrated  $\lambda_{\min}$  using a compression test with fixed bound-  
 ary conditions on the top and bottom to produce barreling and inhomogeneous stress. Fig.4  
 compares the tuned PD response to the compression limit. The black line is the PD response with  
 no compression stretch limit ( $\lambda_{\min} \rightarrow \infty$ ). The inset shows the damage field for the  $4\text{cm} \times 8\text{cm}$   
 325 test specimen.

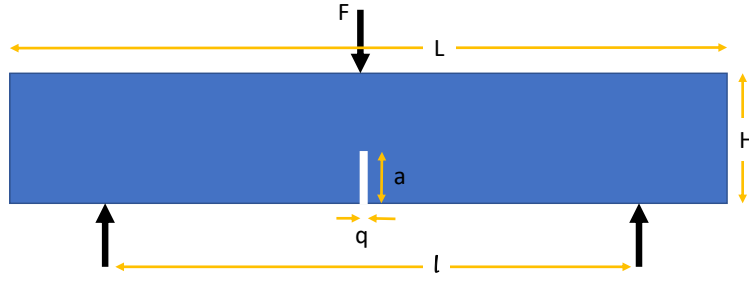


Figure 2: Three point bend geometry

#### 4.1.2. Shrinkage

To calibrate the volumetric shrinkage  $\vartheta$  we employed a cylindrical domain with an inner degraded region and a free surface. To obtain an analytic solution we assume a radial displacement  $\mathbf{u} = u(r)\mathbf{e}_r(\theta)$  and reduce Eq. (1) and Eq. (4) to an axisymmetric boundary value problem with radial coordinate  $r$  and circumferential coordinate  $\theta$ . Given that PD is formulated on positions, we employ the differential equation

$$0 = \frac{\partial^2}{\partial r^2}u + \frac{1}{r} \frac{\partial}{\partial r}u - \frac{1}{r^2}u + \vartheta \quad (23)$$

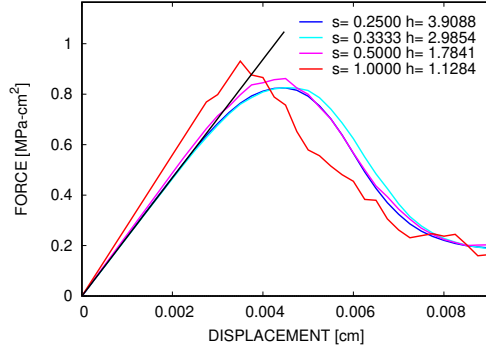


Figure 3: Three point bend load-displacement convergence with respect to point spacing  $s$  and tuned horizon  $h$  for calibrated stiffness  $k$  and tensile stretch limit  $\lambda_{\max}$ . Analytical model (black line) ends at the fracture limit  $F_{\text{peak}}$ .

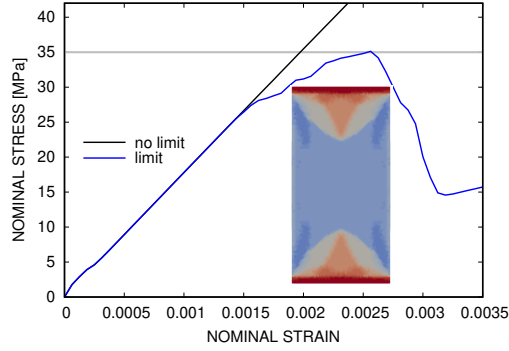


Figure 4: Compression strength: (blue curve) simulation with calibrated compressive stretch limit  $\lambda_{\min}$ , (black curve) simulation without compressive limit, (grey horizontal line) target strength. Inset shows damage field (blue: 1.0, red: 0.0) at nominal strain 0.0003.

governing linear elastic displacements in a cylinder where the inner core  $r < r_i$  shrinks ( $\vartheta < 0$ ) due to degradation and the outer annulus  $r_i < r < r_o$  is pristine ( $\vartheta = 0$ ). We enforce continuity on the displacement and the normal stress and leave the surface free to obtain:

$$u = \begin{cases} \vartheta \frac{(1-2\nu)r_i^2 + r_o^2}{2(1-\nu)r_o^2} r & r < r_i \\ \vartheta \frac{(1-2\nu)r^2 + r_o^2}{2(1-\nu)r_o^2} \frac{r_i^2}{r} & r_i < r < r_o \end{cases}. \quad (24)$$

Fig.5 shows the radial displacement field and compares the PD solution for  $\alpha = -0.002$ ,  $r_i = 2h \approx 1.8$  cm, and  $r_o = 8$ cm, to the analytic solution Eq.(24). The parameter  $\alpha$  needed no adjustment to obtain good correlation with the expected continuum behavior and experimen-

330 tally measured shrinkage.

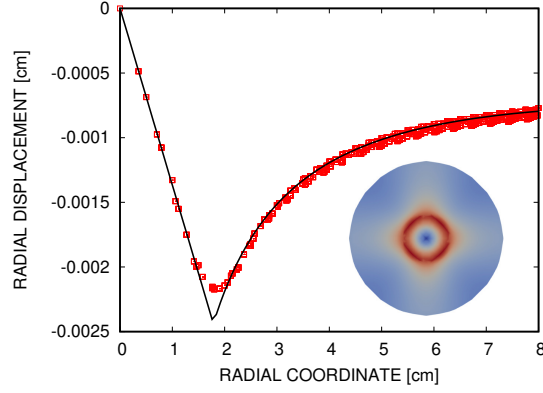


Figure 5: Shrinkage for inner degraded disk and outer pristine annulus. Radial displacement versus radial coordinate (black curve: analytical solution), and (inset) radial displacement field (blue: 0.0, red:-0.00225).

#### 4.1.3. Transport

We calibrate the PD diffusion kernel parameter  $d$  to the experimentally measured diffusivity  $D$  with transient diffusive transport

$$\dot{\tilde{c}} = D \frac{1}{r} \frac{\partial}{\partial r} \left( r \frac{\partial}{\partial r} \tilde{c} \right) \quad (25)$$

with fixed concentration  $\tilde{c} \equiv \tilde{c}_i$  on the inner boundary  $R_i = 1\text{cm}$  and  $\tilde{c} \equiv \tilde{c}_o = 0$  on the outer boundary  $R_o = 11\text{cm}$ . The steady, particular solution is

$$\tilde{c}_\infty(r) = \frac{1}{\ln(R_i/R_o)} (\tilde{c}_i \ln(r/R_o) - \tilde{c}_o \ln(r/R_i)) \quad (26)$$

to which we add a series solution from separation of variables to obtain the full transient solution:

$$\tilde{c}(r, t) = \tilde{c}_\infty(r) + \sum_k \exp(-kDt) \text{Re} [A_k J_0(\imath kr) + B_k Y_0(\imath kr)] \quad (27)$$

where  $J_0$ ,  $Y_0$  are Bessel functions of the first and second kinds and  $A_k$ ,  $B_k$  are the associated coefficients.

335 A comparison of the analytical solution (gray lines) and the PD (color points) simulation is shown in Fig. 6, where the lines generally overlap the points. Clearly, the correspondence is remarkably good given the difference in formulations. The inset of Fig. 6 shows the full field steady solution.

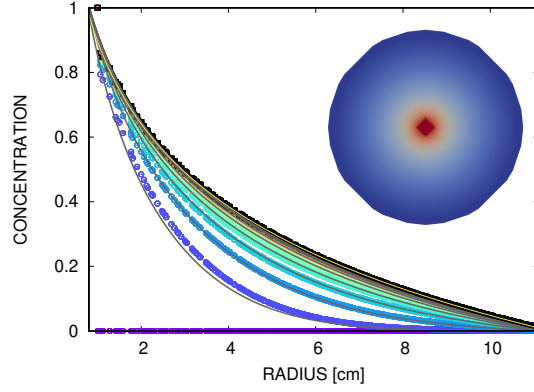


Figure 6: Water diffusion due to a point source in a circular domain: concentration evolution (gray lines: analytic solution, colored points: PD simulation), and (inset) steady concentration field (blue: 0.0, red:1.0).

#### 4.1.4. Reaction

The information available to calibrate the reaction characteristics of the model is more sparse and qualitative than the mechanical and transports aspects. We have estimated the reaction time constant  $K$  in Table 1, which is on the order of 1 month, and the reaction front width, which appears to be on the order of 0.1-1cm [46, 19, 20] at about 1 month in laboratory conditions. Hence we assume that the reaction front keeps pace with the diffusion front and the front width is on the order of our selected resolution  $s=0.5\text{cm}$ .

To simplify interpretation, we employ a quasi-1D calibration problem 40 cm long with a fixed concentration at one end and an impermeable boundary at the other. Using the value of  $K$  in Table 1 and the step treatment in Sec. A.2, Fig. 7 shows that the reaction front is essentially coincident with the diffusion front, as desired. These results compare favorably to the profiles shown in Haga *et al.* Fig. 14 [20] where we have translated the experimentally observed solid calcium concentration to the solid state variable  $\underline{c}$ .

#### 4.2. Demonstration

As part of validation of the model and to illustrate the qualitative behavior of our fully coupled chemomechanical model, we revisit the three point beam bending of Sec. 4.1.1 using the nominal properties in Table 1. We vary the duration of the simulation to explore the relative importance of the external mechanical loading and the evolution of the chemical reactive-diffusive process originating at the (1 cm) notch in the middle of the lower surface of the beam. In these simulations

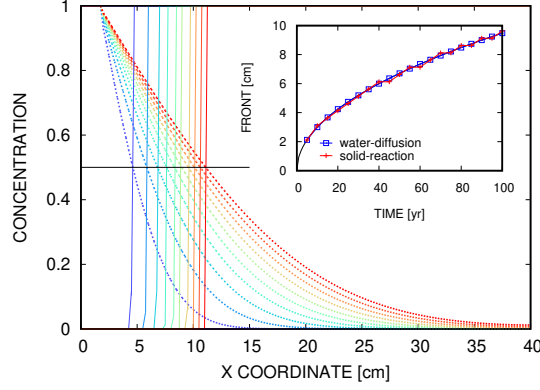


Figure 7: Reaction-diffusion fronts due to an end source on a quasi-one dimensional domain: concentration (dashed lines) and reaction (solid lines) profiles for a sequence of times ( blue: 10 yr, red: 100 yr) and inset shows the diffusion and reaction front locations versus time. Note the fluid  $\tilde{c}$  (dashed lines) and solid  $\underline{c}$  (solid lines) concentrations are non-dimensional and range from 0 to 1.

we increase the number of flow steps in Eq. (A.59) and Eq. (A.61) between every displacement solve Eq. (A.60) starting with  $m=0$  and going up to 80 with a time step of  $\Delta t = 0.01$  year.

Since shrinkage seemed to be the most influential property we explored three cases: (a) no shrinkage ( $\alpha = 0$ ), (b) full shrinkage ( $\alpha = -0.002$ ), and (c) reduced shrinkage ( $\alpha = -0.0004$ , 1/5 of nominal). The force-displacement curves for these three cases for the three-point beam bending are shown in Fig. 8 for a variety of loading rates. For the no shrinkage case we see a general decrease in maximum force with little change in the flexural modulus. The short duration simulation provides an exception where the maximum load is slightly higher than the (effectively) instantaneous simulation and the energy absorbed is significantly higher. This suggests mechanisms competing over different timescales. The full shrinkage case also displays some evidence of competing mechanisms where the short duration simulation fails below the instantaneous baseline simulation, while the remainder display increasing flexural modulus and lower peak load with longer durations. The increase in flexural modulus is curious and will be explored in more detail. The intermediate, reduced shrinkage case displays trends that are typical of (shorter duration) experiments: decreasing peak load and lower total displacement with increasing degradation.

Comparing these results to Le Bellégo *et al.* [43], we see a similar trend with degradation and the relative changes in the flexural modulus can be attributed to the differences in the degraded zones. In Ref. [43] the entire lower surface is exposed to reacting fluid, whereas in our simulations

only a region near the notch is affected for most conditions. Qualitatively, the force-displacement  
 375 response shown in Ref. [41] Fig. 6 and Ref. [43] Fig. 6 display similar broadening and lowering of  
 the peak load with increased Ca leaching. This behavior is fairly general, in that it is also observed  
 in the investigations of Giaccio *et al.* [103] and Pignatelli *et al.* [44] for the alkali-silica reaction of  
 concrete. We can also compare to the compression experiments of Nguyen *et al.* [118] which show a  
 high maximum load and brittle behavior transitioning to lower maximum load and more toughness  
 380 with longer exposure of the hollow concrete aggregate cylinders to an ammonium nitrate solution.

Given the somewhat surprising behavior of the full shrinkage case, we also examined the water  
 concentration (range 0:blue to 1:red in Fig. 9 through Fig. 14) and the 11-deformation gradient  
 fields (red: -0.00001, blue: 0.00001). Note that, given the reaction rate relative to the diffusion  
 speed, the area with water infiltration is effectively coincident with the degraded zone in all but  
 385 the fastest loadings. Also note that the deformation gradient is calculated with respect to original,  
 undeformed configuration, and, with reference to Eq. (4), is composed of both the shrinkage strain  
 and the elastic strain. This strain field is effective in identifying the crack (red dot at crack tip)  
 and the mechanically degraded region (reddish semi-disk) which can subsume the crack.

For the no shrinkage condition, comparing a short duration case, Fig. 9, to a long duration case,  
 390 Fig. 10, we expected differences in the diffusion progression and qualitative differences in the strain  
 fields. For the short duration case Fig. 9, we observe a localized softened zone near the notch that  
 progresses slowly and is eventually outstripped by the propagation of the fracture (evidenced by  
 the bump that appears at the top of the semicircular degraded zone in the strain field). The long  
 duration case Fig. 9 on the other-hand, shows more pervasive progression of water infiltration and a  
 395 qualitatively different strain pattern. In this case the degradation region progresses to boundaries,  
 fracture does not progress outside the softened zone, and the strain field indicates increased bending  
 in the softened middle section of the beam. These cases illustrate the competition between the longer  
 time-scale softening and the shorter time-scale, more brittle fracture propagation where the induced  
 crack moves ahead of the degradation front. The short duration simulation, where local softening  
 400 that increases effective toughness, differs qualitatively from the instantaneous simulation, where the  
 main effect is the crack progress decreasing the effective beam height. We also observe that water  
 follows the crack based on damage criterion and dynamic boundary condition described in Sec. A.3.  
 (This is particularly apparent in the instantaneous case, which is not shown for brevity.)

For the two cases with shrinkage the corresponding water and strain fields generally resemble

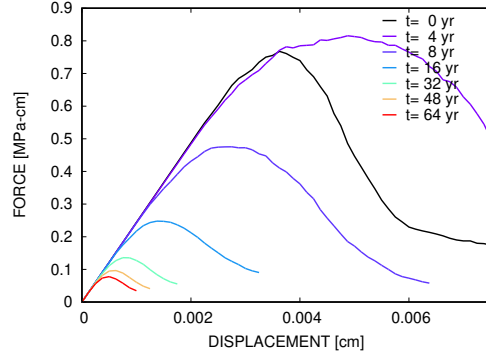


each other, with the short duration simulations failing later than the long duration simulations due to chemical degradation effects. In these cases the degradation/shrinkage strain  $\mathcal{O}(\alpha) = 10^{-3}$  typically dominates the elastic strain  $-10^{-3} < \lambda < 10^{-6}$  (which is asymmetric due to the different tension-compression behavior of HCP) so that the stress in the degraded area outlined by water infiltration is dominated by tension. Locally these shrinkage strains are also much larger than the strains induced by beam flexure by the external forces. In both the short and long duration simulations of these cases, the water progression pattern is similar and the strain pattern in the degraded region displays an outer tensile region and an inner compressive region not observed in the no shrinkage cases. Interestingly, in Fig. 13 and Fig. 14 a lobed pattern in the strain is apparent. In the shrinkage cases this compressive region is created by the degraded region tending to shrink but being constrained by the boundary conditions. This phenomenon leads to the increases in the observed flexural modulus of the beam for the extreme cases. Since this less stiff region encompasses the crack, crack propagation is also inhibited in the extreme cases. In summary, the interplay between reaction-diffusion driven shrinkage and mechanical loading lead to complex stress states near an imperfection even for a simple beam and the outcomes depend strongly on the rate of the mechanical loading relative to the diffusion process. Generally speaking, the chemical degradation leads to softening of the beam flexure and a lower and earlier peak load.

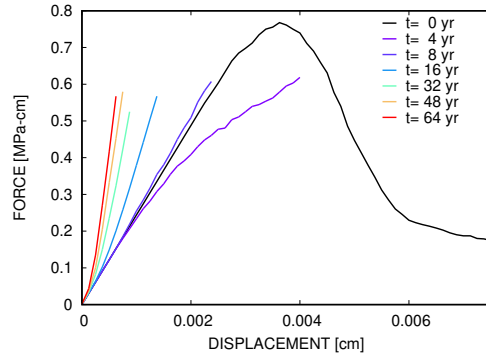
### 4.3. Prediction

We now use the calibrated model to make predictions. Without experimental measurements to the contrary, we assume the material parameters in Table 1 that define the physical response are uncorrelated. Since we generally only know minimum and maximum measured values circumscribing a range of properties, the maximum entropy principle [124, 125] justifies using the uniform distributions given in Table 3. Although we assume the material properties are independent, the scaling of PD parameters summarized in Table 2 induce interdependencies in the parameters. For instance, the critical tensile stretch  $\lambda_{\max}$  is the result of two uncorrelated uniform variables, namely the Young's modulus  $E$  and the fracture toughness  $K_{Ic}$ . Since we are interested in sensitivities to material properties, not model parameters, we sample the pristine property and the degraded difference ( $E$  and  $\Delta E$  for instance), from Table 3 and use Table 2 to map these values to the corresponding PD parameters.

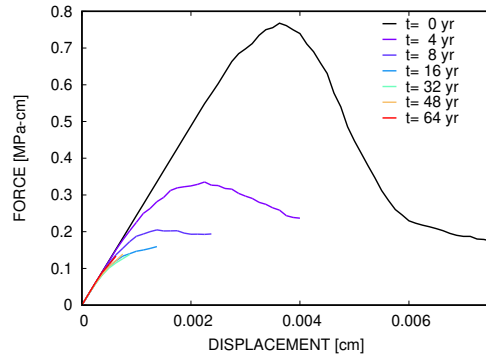
We use a simplified simulation of a bridge support for exploration of what properties are the



(a) no shrinkage



(b) full shrinkage



(c) reduced shrinkage

Figure 8: Change in mechanical response with loading duration  $t = \{0, 4, 8, 16, 32, 48, 64\}$  year to reach 0.001 cm applied displacement of the center of the three point beam bending.

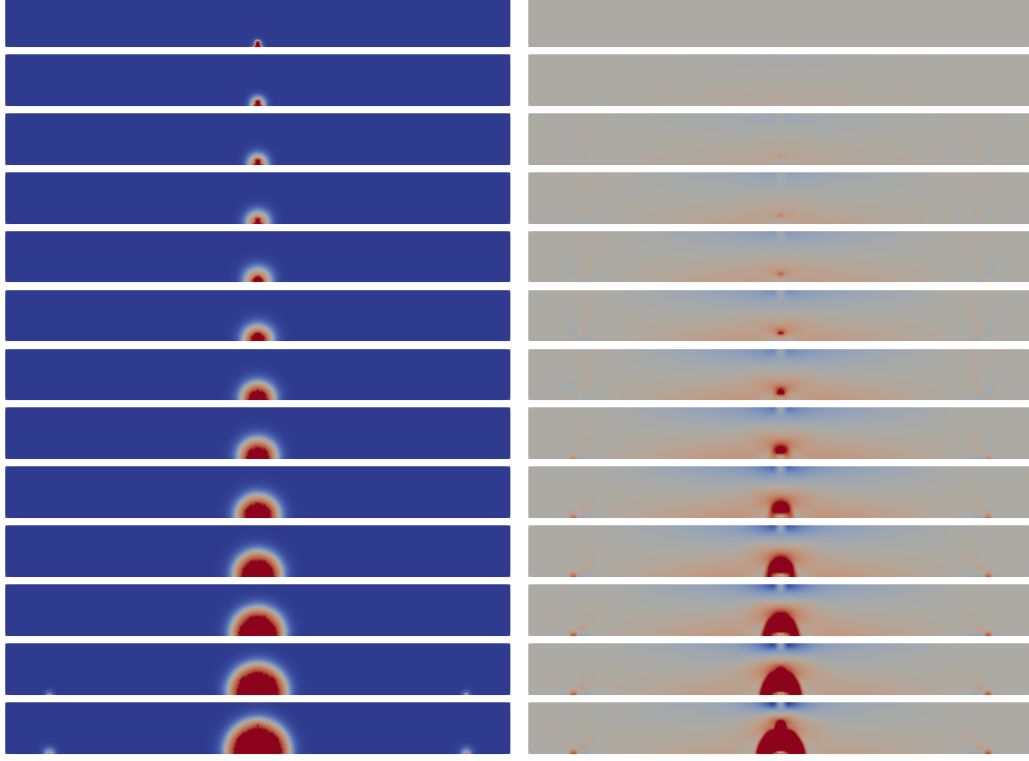


Figure 9: Loading rate 0.01/4 cm/yr for no shrinkage case: water infiltration (left, blue: 0.0, red: 1.0) and 11 deformation gradient (right, blue:  $-10^{-5}$ , red:  $10^{-5}$ ). Fields are displayed every 0.0001250 cm of displacement.

determining effects of fracture and failure and their variability. We employ a vertical 4cm $\times$ 24cm simply supported beam under static load that pre-compresses the beam to 10 % of failure at nominal strain ( $\sigma_c/E \approx 0.12$  %). The beam is also under chemical attack at a point midway up on one side due to a localized water source modeling a permeable (non-mechanical) flaw in the surface. At first some of the bonds in the model break, then the beam starts to fracture, and eventually the beam fails in compressive buckling. Fig. 15 shows the support for typical parameters as it starts to buckle (the flaw is at the midpoint of the right side of the support). The simulations with a sampling of the various parameters are run with a flow time step of  $\Delta t = 0.001$  year and stress solves every 2 time steps to capture differences in failure on this time-scale. We select two quantities of interest (QoIs): (a) the time to first bond breakage  $t_f$  which we associate with fracture and (b) the time to total failure  $t_F$  where the structure becomes unstable.

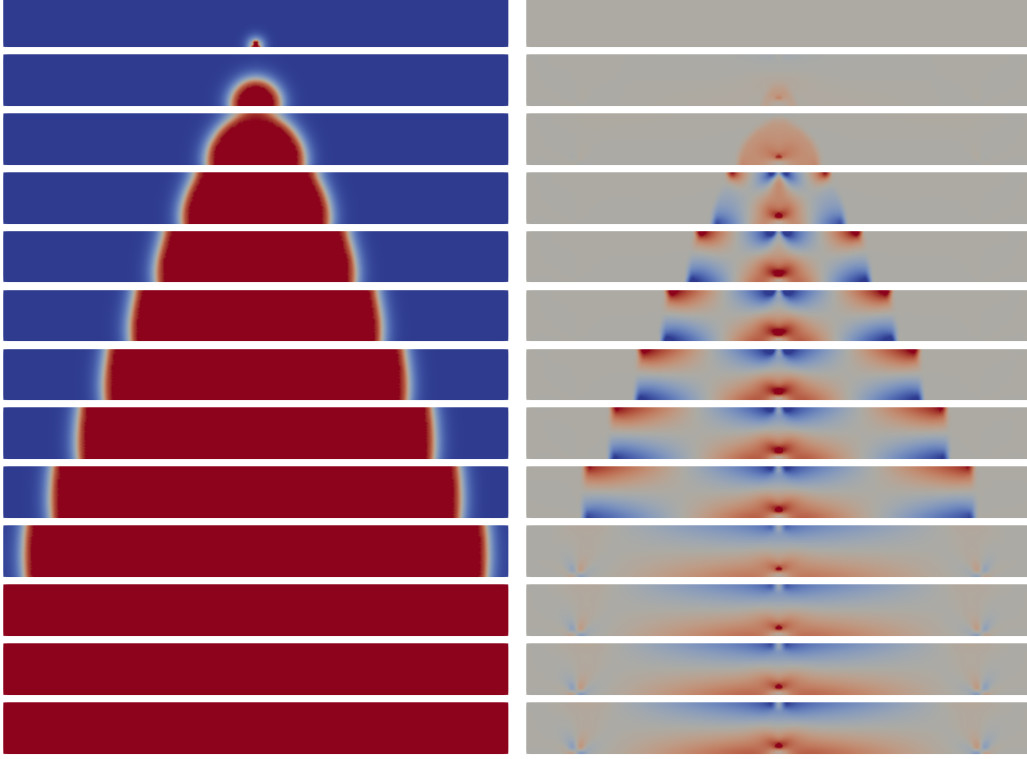


Figure 10: Loading rate 0.01/48 cm/yr for no shrinkage case: water infiltration (left, blue: 0.0, red: 1.0) and 11 deformation gradient (right, blue:  $-10^{-5}$ , red:  $10^{-5}$ ). Fields are displayed every 0.0001250 cm of displacement starting at the top.

#### 4.3.1. Sensitivity

We explore the sensitivities of the QoIs to the material parameters using traditional local derivative and global variance-based (Sobol) sensitivities [126]. Local sensitivities are essentially derivatives of the QoIs with respect to the inputs at specific input values. Here we evaluate the differences in the QoIs at the upper versus the lower bound of a particular parameter in Table 3, while the other parameters are fixed at their median values. Unlike local sensitivities, global sensitivities measure influence in terms of distributions [127]. Sobol sensitivities are based on a decomposition of the variance of the output QoIs in terms of the inputs (properties). First order sensitivities  $S_i$  are essentially the fraction of total variance due to varying one parameter over its expected distribution

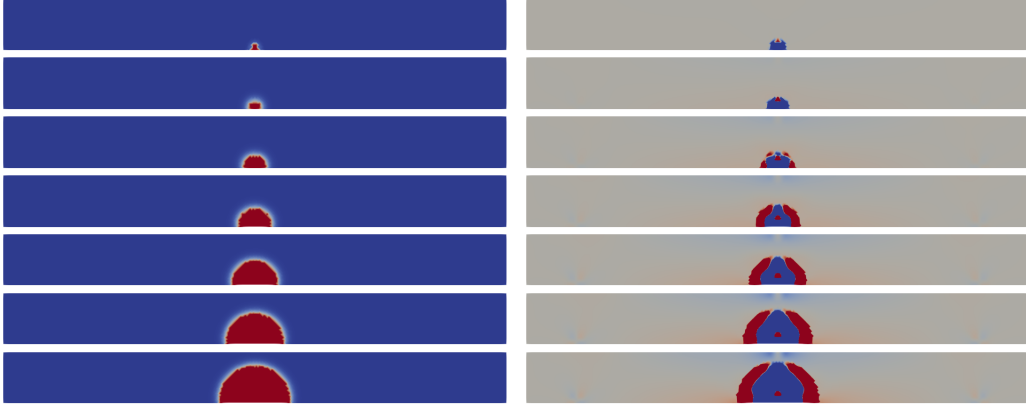


Figure 11: Loading rate 0.01/4 cm/yr for the full shrinkage case: water infiltration (left, blue: 0.0, red: 1.0) and 11 deformation gradient (right, blue:  $-10^{-5}$ , red:  $10^{-5}$ ). Fields are displayed every 0.0001250 cm of displacement starting at the top.



Figure 12: Loading rate 0.01/48 cm/yr for the full shrinkage case: water infiltration (left, blue: 0.0, red: 1.0) and 11 deformation gradient (right, blue:  $-10^{-5}$ , red:  $10^{-5}$ ). Fields are displayed every 0.0001250 cm of displacement starting at the top.

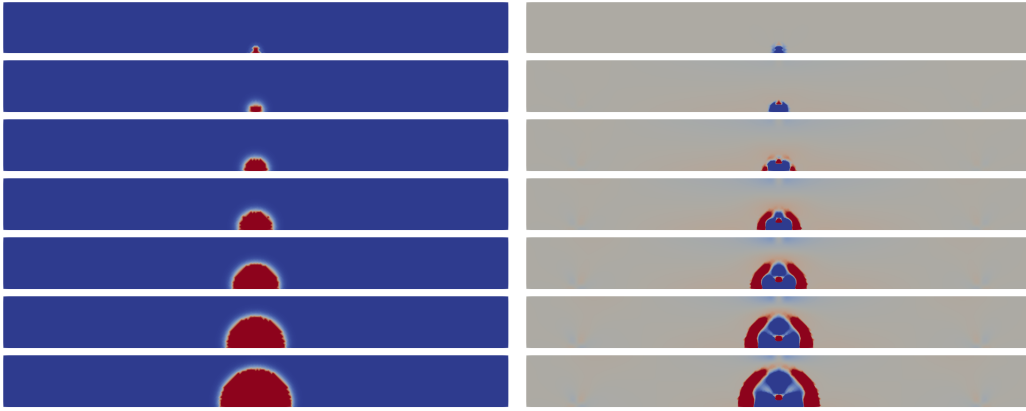


Figure 13: Loading rate 0.01/4 cm/yr for the reduced shrinkage case: water infiltration (left, blue: 0.0, red: 1.0) and 11 deformation gradient (right, blue:  $-10^{-5}$ , red:  $10^{-5}$ ). Fields are displayed every 0.0001250 cm of displacement starting at the top.



Figure 14: Loading rate 0.01/48 cm/yr for the reduced shrinkage: water infiltration (left, blue: 0.0, red: 1.0) and 11 deformation gradient (right, blue:  $-10^{-5}$ , red:  $10^{-5}$ ). Fields are displayed every 0.0001250 cm of displacement starting at the top.

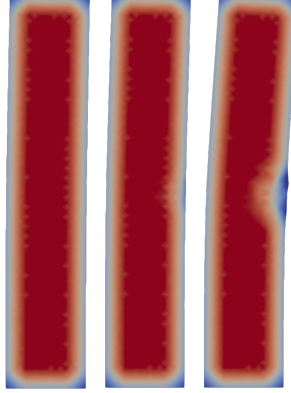


Figure 15: Support starting to buckle ( $t=0.6, 0.7, 0.8$  yr) after being subjected to chemical attack at a point midway on the right side. Support is colored by the damage field (blue: 1.0, red: 0.0). Note that surfaces (existing and newly created) are colored blue since particles there have lower coordination than in the interior of the beam.

averaged over the distribution of the other parameters:

$$S_i = \frac{\mathbb{V}_i[\mathbb{E}_{\forall j \neq i}[q|\theta_j]]}{\mathbb{V}[q]} \quad (28)$$

where  $\theta_i \in \{E, \Delta E, K_{Ic}, \dots\}$  and  $q \in \{t_f, t_F\}$ . Second order sensitivities  $S_{ij}$  measure the joint contribution of two parameters while subtracting the corresponding first order sensitivities. Refer to Ref. [127] for more details.

450 Fig. 16a plots the local parametric sensitivities and shows the changes in the fracture and failure times due to each of the properties taking on their minimum and maximum values while holding the remaining properties at their median values. For the given ranges in Table 3 it appears that the diffusion,  $D$  and  $\Delta D$ , and reaction,  $K$  and  $\Delta K$ , parameters effect most change in failure times while the mechanical parameters have much smaller effects. Increases in these chemical properties result  
455 decreased lifetimes. This, in part, reflects the uncertainty in these parameters which determine the minimum and maximum parameter values considered. Furthermore, the effects on the failure

Property	Pristine		Degradation	
Young's modulus [GPa]	$E$	[23,34]	$\Delta E$	[-18,-20]
Fracture toughness [MPa-cm <sup>1/2</sup> ]	$K_{Ic}$	[2.5,3.0]	$\Delta K_{Ic}$	[-0.7,-0.8]
Compressive strength [MPa]	$\sigma_c$	[30,41]	$\Delta \sigma_c$	[-9,-8]
Diffusivity [cm <sup>2</sup> /yr]	$D$	[0.026,3.7]	$\Delta D$	[5.8,24.8]
Reaction rate <sup>†</sup> [1/yr]	$K$	[18,33]	$\Delta K$	[29,33]
Radial shrinkage	$\alpha$	0.0	$\Delta \alpha$	[0.0018,0.0022]

Table 3: Distribution of pristine and degradation properties. All assumed to be uniform distributions defined by the listed lower and upper bounds.

versus fracture times for the parameters that significantly affect the QoIs are roughly proportional to the ratio of the mean fracture time (0.239 yr) to the mean fail time (0.685 yr).

To estimate variance-based sensitivities  $S_i$  and  $S_{ij}$ , which are summarized in Fig. 16b and Fig. 17, we performed 240,000 independent simulations sampling the input distributions summarized in Table 3. The first order property sensitivities shown in Fig. 16 indicate the fracture and failure times are sensitive to almost all parameters over the given ranges. As with local sensitivities, the chemical and transport parameters are generally more influential than the mechanical parameters given the respective uncertainties; however, as indicated in the beam bending study, the shrinkage is the dominant effect. Also it appears that variations in the changes with degradation of the mechanical properties, such as  $\Delta K_{Ic}$  and to a lesser extent  $\Delta \sigma_c$  and  $\Delta E$ , have a greater effect on the time to fracture and failure. In fact, the influence of  $E$ ,  $K_{Ic}$  and  $\sigma_c$  are nearly negligible in this regard. Le Bellégo *et al.* [119] observed some corroborating behavior. They saw that the time to failure was extremely sensitive to the fracture energy ( $K_{Ic}$ ) and (compressive) strength ( $\sigma_c$ ) relative to the elastic modulus ( $E$ ). (Note that first order Sobol sensitivities, as ratios of variances can not be negative so the two negative sensitivities in Fig. 16b are likely due to sampling error; since they persisted in going from 24,000 to 240,000 samples we assume they are due to only being able to sample the failure times at discrete intervals.) With reference to Fig. 17 the correlated effects are positive and fairly small with largest effect associated with the interactions shrinkage  $\alpha$  with the other parameters. Also, the second order sensitivities are nearly identical for time to first breakage as they are for the time to failure suggesting a scaling relationship.

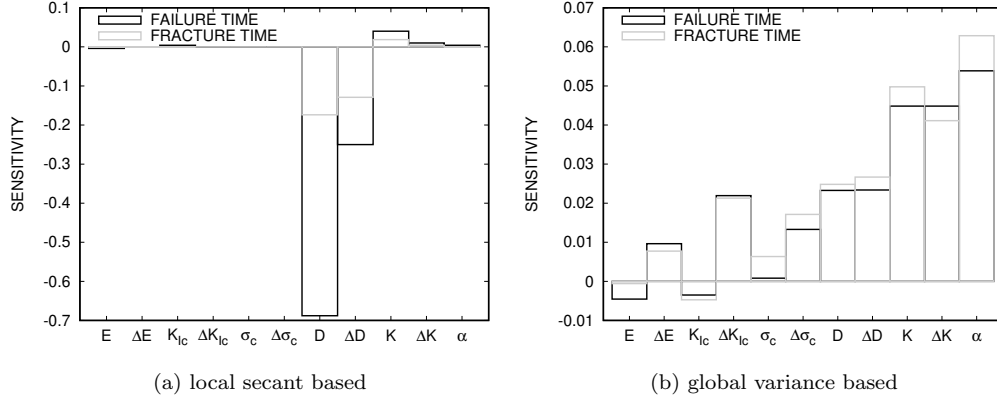


Figure 16: Local (secant) and global (variance) primary (first order) sensitivities of time to fracture and failure to the selected material properties. Local sensitivities are given in years. Global sensitivities are non-dimensional.

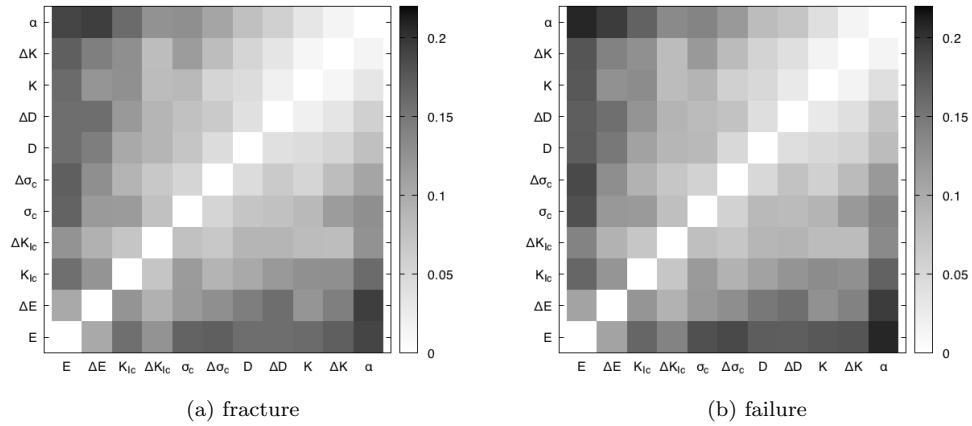


Figure 17: Cross parameter second order sensitivities for time to fracture and time to failure

#### 4.3.2. Uncertainty

Since the preceding sensitivity analysis showed that generally all properties contribute to the two quantities of interest, we examine the distribution of the two QoIs over the distribution of all the properties. Since we have assumed that the input properties are independent and uniformly distributed sampling them is straightforward.

To obtain the distributions shown in Fig. 18 we performed 20,000 independent simulations drawing parameter values using Latin hypercube sampling (LHS) [128, 129]. The joint distribution of



the two QoIs shown in Fig. 18a indicates the time to fracture and the time to failure are strongly correlated and that there is significant variance in the outcomes. Marginal distributions of the two QoIs and their difference in Fig. 18b resemble log-normal distributions and show a steep onset for both the time-to-fracture and the time-to-failure, and particularly long tail to time to failure distribution. The long tails suggest that some structures, with particularly fortuitous combinations of physical properties, can have lifetimes that far exceed the mean. The mean time to fracture is 0.239 year, the mean time to failure is 0.685 year, and the mean difference in the onset to culmination of failure is 0.446 year. The strong correlation suggests that initial fractures can indicate impending failure; and, despite the overlap in the distributions, the distribution of the difference in the two QoIs indicates that there would be at almost a half a year on average and at least a tenth of year of warning time.

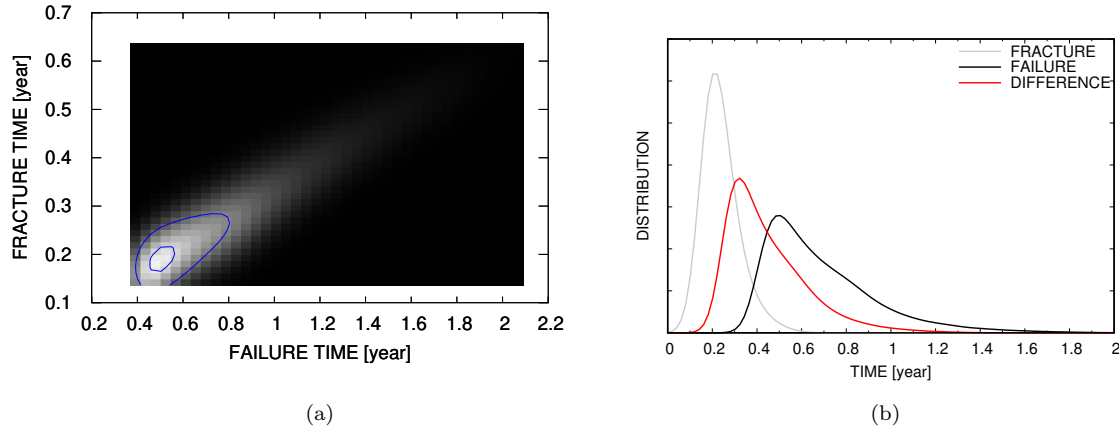


Figure 18: Uncertainty of time to fracture and failure: (a) joint distribution, and (b) and marginal distributions. Note that the normalized distributions are in units of  $[1/\text{year}]$ .

## 5. Conclusion

We developed a chemomechanical model of the main phenomenological effects of water induced degradation of hardened cement paste (HCP), including; softening, weakening, swelling, increased fluid transport and increased reactivity. The model couples the mechanical static equilibrium balance with reactive-diffusive transport and incorporates large-scale fracture and failure via peri-

500 dynamics (a meshless method). Using a variety of analytic solutions to two-dimensional boundary  
 value problems emulating common mechanical and reaction-diffusion tests, we calibrated the model  
 to experimental property measurements from the initial stage of HCP degradation, decalcification  
 of CH. The correspondence of the simulations to calibrate shrinkage and reaction-diffusion with  
 expectations from experiments and analytical solutions was remarkable after tuning the mechani-  
 505 cal properties and PD horizon to the selected resolution. Comparison of the validation simulation  
 Sec. 4.2 directly with existing experimental tests was hampered by (a) two dimensional implementa-  
 tion of the model, (for example, in the beam bending experiment of Le Bellégo *et al.* [41] chemical  
 attack was only allow on the lateral/out-of-plane sides of the beam), (b) the indirect and incomplete  
 characterization of the chemical species diffusion and reaction, and (c) the lack of a consistent set  
 510 of experimental measurements across all the properties the model simulates. We addressed these  
 issues by forming a physically motivated phenomenological model, rather than a detailed microme-  
 chanical one, and calibrated it to observed data. The subsequent predictions should be taken in  
 light of the qualitative nature of the validation. This simulation did serve to demonstrate that the  
 behavior of a simple beam in bending can change dramatically depending on whether the mechan-  
 515 ical process is fast or slow relative to the chemical process. To the last point (c), the uncertainty  
 quantification was presented largely to address the variability/inconsistency of the experimental  
 measurements and to demonstrate the value of UQ has in predicting high consequence events such  
 as bridge failure.

Ultimately, we demonstrated that the model and method are capable of plausible predictions  
 520 of long-term failure of cement-based structures. The flexural bending and compressive beam fail-  
 ure results indicate high sensitivity to shrinkage and competing mechanisms for weakening of the  
 HCP. Uncertainty quantification (UQ) of eleven distinct parameters and their cross terms were  
 investigated. The computational cost of the UQ motivated the two dimensional implementation of  
 the model. Even with the simplified physical model we presented, the sensitivity analysis shows  
 525 complex interplay of mechanisms and reemphasizes the importance of uncertainty quantification in  
 predictions of long-term behavior. Time-to-fracture and time-to-failure generally indicated strong  
 sensitivity to shrinkage, moderate sensitivity to reaction and transport properties, and lower sensi-  
 tivities to mechanical properties, given the assumed uncertainties in these experimentally measured  
 parameters and the model. Practically speaking, the simulations indicated that initial fractures  
 530 can be indications of imminent failure due to the strong correlation between these events and the

time between these events being at least a significant fraction of a year. Larger scale, more detailed simulations of this nature could contribute to infrastructure inspection schedules.

Despite its complexity, there are numerous limitations of the present model due to simplifying assumptions and lack of experimental data, particularly: lumping the mobile species, ignoring precipitation, and the qualitative treatment of the post-peak load and diffusion front behavior. Modeling the post-peak load with more fidelity is straight-forward and can be accomplished by adding a non-zero post-rupture response to the bond force function, albeit with the cost of additional calibration parameters. In future work, we intend to pursue this enhancement and to extend the model to: (a) a more representative reaction model that accounts for changes in pH and the multiple reactions that describe complete degradation, and (b) three dimensions to explore the interactions of complex fracture patterns evoked by more realistic geometry and directly represented with peridynamics. A three dimensional implementation will also facilitate more quantitative comparisons with existing degradation and leaching experiments. More complex reaction-diffusion models exist in the literature [49, 57] as do quantitative descriptions of pH effects and additional reactions such as the alkali-silica reaction [103, 44]. In this work we aimed to develop a model whose complexity matched the depth of the available data; we foresee that a more detailed model could have mechanisms that have confounding effects on observed behavior such as chemically induced shrinkage/expansion [130]. Details of the pore porosity and permeability distribution are undoubtedly more intricate and influential than we were able to resolve but, as stated, we aimed for a minimally complex model that could be calibrated to existing data. These micromechanical mechanisms are largely uncharacterized experimentally and would be expensive to characterize in built infrastructure. In addition, we could add poroelastic effects with strong coupling between structure and fluid, pressure driven flow [75] and viscoelasticity/creep [131, 132, 133, 134]. In ambient conditions there typically are not high pressure gradients; however, viscous effects are particularly important in the long term behavior of statically loaded components. Ultimately we wish to validate the model via predictions of truly long term, “natural” experiments such as the parking structure failure documented in Ref. [135] and the 12 year study described in Ref. [136].

## Acknowledgments

This work was supported by the Laboratory Directed Research and Development program at Sandia National Laboratories (project 213007). Sandia National Laboratories is a multimission

laboratory managed and operated by National Technology and Engineering Solutions of Sandia, LLC., a wholly owned subsidiary of Honeywell International, Inc., for the U.S. Department of Energy's National Nuclear Security Administration under contract DE-NA0003525. The views expressed in the article do not necessarily represent the views of the U.S. Department of Energy or the United States Government.

## References

- [1] S. Hanna, R. Jones, Composite wraps for aging infrastructure: Concrete beams, *Engineering Failure Analysis* 4 (3) (1997) 215–225.
- [2] R. Pinto, S. Hobbs, K. Hover, et al., Accelerated aging of concrete: a literature review, Tech. rep., Turner-Fairbank Highway Research Center (2002).
- [3] F. Chughtai, T. Zayed, Infrastructure condition prediction models for sustainable sewer pipelines, *Journal of Performance of Constructed Facilities* 22 (5) (2008) 333–341.
- [4] V. Kumar, Protection of steel reinforcement for concrete-a review, *Corrosion reviews* 16 (4) (1998) 317–358.
- [5] S. Yang, X. Xi, K. Li, C.-Q. Li, Numerical modeling of nonuniform corrosion-induced concrete crack width, *Journal of Structural Engineering* 144 (8) (2018) 04018120.
- [6] J. Zhao, Z. Chen, J. Mehrmashhadi, F. Bobaru, A stochastic multiscale peridynamic model for corrosion-induced fracture in reinforced concrete, *Engineering Fracture Mechanics* (2020) 106969.
- [7] W. Kurdowski, The protective layer and decalcification of CSH in the mechanism of chloride corrosion of cement paste, *Cement and Concrete Research* 34 (9) (2004) 1555–1559.
- [8] K. L. Scrivener, Backscattered electron imaging of cementitious microstructures: understanding and quantification, *Cement and concrete Composites* 26 (8) (2004) 935–945.
- [9] H. F. Taylor, et al., *Cement chemistry*, Vol. 2, Thomas Telford London, 1997.
- [10] S. Mindess, F. Young, D. Darwin, *Concrete* 2nd editio, Technical Documents (2003).

- [11] U. Birnin-Yauri, S. Garba, The effect and mechanism of chloride ion attack on portland cement concrete and the structural steel reinforcement, *Ife Journal of Science* 8 (2) (2006) 131–134.
- [12] B. Johannesson, K. Yamada, L.-O. Nilsson, Y. Hosokawa, Multi-species ionic diffusion in concrete with account to interaction between ions in the pore solution and the cement hydrates, *Materials and structures* 40 (7) (2007) 651.
- [13] M. Zhang, J. Chen, Y. Lv, D. Wang, J. Ye, Study on the expansion of concrete under attack of sulfate and sulfate–chloride ions, *Construction and Building Materials* 39 (2013) 26–32.
- [14] L. Urbonas, V. Leno, D. Heinz, Effect of carbonation in supercritical co<sub>2</sub> on the properties of hardened cement paste of different alkalinity, *Construction and Building Materials* 123 (2016) 704–711.
- [15] J. Perko, K. U. Mayer, G. Kosakowski, L. De Windt, J. Govaerts, D. Jacques, D. Su, J. C. Meeussen, Decalcification of cracked cement structures, *Computational Geosciences* 19 (3) (2015) 673–693.
- [16] M. Paul, F. Glasser, Impact of prolonged warm (85 c) moist cure on portland cement paste, *Cement and Concrete Research* 30 (12) (2000) 1869–1877.
- [17] I. Segura, M. Molero, S. Aparicio, J. Anaya, A. Moragues, Decalcification of cement mortars: Characterisation and modelling, *Cement and Concrete Composites* 35 (1) (2013) 136–150.
- [18] J. Thomas, D. Neumann, J. Chen, H. Jennings, Ca-OH bonding in decalcified portland cement and tricalcium silicate pastes measured by inelastic neutron scattering, *Chem. Mater* 15 (2003) 3813–3817.
- [19] K. Haga, M. Shibata, M. Hironaga, S. Tanaka, S. Nagasaki, Change in pore structure and composition of hardened cement paste during the process of dissolution, *Cement and Concrete Research* 35 (5) (2005) 943–950.
- [20] K. Haga, S. Sutou, M. Hironaga, S. Tanaka, S. Nagasaki, Effects of porosity on leaching of Ca from hardened ordinary portland cement paste, *Cement and Concrete Research* 35 (9) (2005) 1764–1775.

- [21] G. Constantinides, F.-J. Ulm, The effect of two types of CSH on the elasticity of cement-based materials: Results from nanoindentation and micromechanical modeling, Cement and concrete research 34 (1) (2004) 67–80.
- [22] J. J. Chen, J. J. Thomas, H. M. Jennings, Decalcification shrinkage of cement paste, Cement and concrete research 36 (5) (2006) 801–809.
- [23] H. Yu, J. Yang, H. Rong, Research on decalcification degradation process of cement stone, Journal of Wuhan University of Technology-Mater. Sci. Ed. 30 (2) (2015) 369–374.
- [24] F. P. Glasser, J. Marchand, E. Samson, Durability of concrete—degradation phenomena involving detrimental chemical reactions, Cement and Concrete Research 38 (2) (2008) 226–246.
- [25] M. H. Beygi, M. T. Kazemi, I. M. Nikbin, J. V. Amiri, The effect of water to cement ratio on fracture parameters and brittleness of self-compacting concrete, Materials & Design 50 (2013) 267–276.
- [26] K. Y. Cheng, P. L. Bishop, Morphology and pH changes in leached solidified/stabilized waste forms, in: Stabilization and Solidification of Hazardous, Radioactive, and Mixed Wastes: 3rd Volume, ASTM International, 1996.
- [27] H. Dehwah, Effect of sulfate concentration and associated cation type on concrete deterioration and morphological changes in cement hydrates, Construction and Building Materials 21 (1) (2007) 29–39.
- [28] C. Carde, R. Francois, J.-M. Torrenti, Leaching of both calcium hydroxide and CSH from cement paste: Modeling the mechanical behavior, Cement and concrete research 26 (8) (1996) 1257–1268.
- [29] C. Carde, R. François, Effect of the leaching of calcium hydroxide from cement paste on mechanical and physical properties, Cement and Concrete Research 27 (4) (1997) 539–550.
- [30] C. Carde, R. Francois, Modelling the loss of strength and porosity increase due to the leaching of cement pastes, Cement and Concrete Composites 21 (3) (1999) 181–188.

- [31] H. Saito, A. Deguchi, Leaching tests on different mortars using accelerated electrochemical method, *Cement and Concrete Research* 30 (11) (2000) 1815–1825.
- [32] F. Agostini, Z. Lafhaj, F. Skoczylas, H. Loodsveldt, Experimental study of accelerated leaching on hollow cylinders of mortar, *Cement and Concrete Research* 37 (1) (2007) 71–78.
- [33] A. Babaahmadi, L. Tang, Z. Abbas, P. Mårtensson, Physical and mechanical properties of cementitious specimens exposed to an electrochemically derived accelerated leaching of calcium, *International Journal of Concrete Structures and Materials* 9 (3) (2015) 295–306.
- [34] J. Jain, N. Neithalath, Analysis of calcium leaching behavior of plain and modified cement pastes in pure water, *Cement and Concrete Composites* 31 (3) (2009) 176–185.
- [35] Z. Makhloufi, E. Kadri, M. Bouhicha, A. Benaissa, R. Bennacer, The strength of limestone mortars with quaternary binders: Leaching effect by demineralized water, *Construction and Building Materials* 36 (2012) 171–181.
- [36] B. Gerard, G. Pijaudier-Cabot, C. Laborderie, Coupled diffusion-damage modelling and the implications on failure due to strain localisation, *International Journal of Solids and Structures* 35 (31-32) (1998) 4107–4120.
- [37] S. Kamali, B. Gérard, M. Moranville, Modelling the leaching kinetics of cement-based materials—influence of materials and environment, *Cement and Concrete Composites* 25 (4-5) (2003) 451–458.
- [38] D. Planel, J. Sercombe, P. Le Bescop, F. Adenot, J.-M. Torrenti, Long-term performance of cement paste during combined calcium leaching–sulfate attack: kinetics and size effect, *Cement and Concrete Research* 36 (1) (2006) 137–143.
- [39] Q. T. Phung, N. Maes, D. Jacques, G. De Schutter, G. Ye, Investigation of the changes in microstructure and transport properties of leached cement pastes accounting for mix composition, *Cement and Concrete Research* 79 (2016) 217–234.
- [40] K. Wan, L. Li, Q. Xu, W. Sun, Spatial distribution of the increased porosity of cement paste due to calcium leaching, *Journal of Wuhan University of Technology-Mater. Sci. Ed.* 30 (4) (2015) 735–744.

- [41] C. L. Bellégo, B. Gérard, G. Pijaudier-Cabot, Chemo-mechanical effects in mortar beams subjected to water hydrolysis, *Journal of engineering mechanics* 126 (3) (2000) 266–272.
- [42] B. Gérard, C. Le Bellego, O. Bernard, Simplified modelling of calcium leaching of concrete in various environments, *Materials and Structures* 35 (10) (2002) 632–640.
- 670 [43] C. Le Bellégo, G. Pijaudier-Cabot, B. Gérard, J.-F. Dubé, L. Molez, Coupled mechanical and chemical damage in calcium leached cementitious structures, *Journal of Engineering Mechanics* 129 (3) (2003) 333–341.
- [44] R. Pignatelli, C. Comi, P. J. Monteiro, A coupled mechanical and chemical damage model for concrete affected by alkali–silica reaction, *Cement and Concrete Research* 53 (2013) 196–210.
- 675 [45] O. Coussy, F.-J. Ulm, Creep and plasticity due to chemo-mechanical couplings, *Archive of Applied Mechanics* 66 (8) (1996) 523–535.
- [46] F.-J. Ulm, J.-M. Torrenti, F. Adenot, Chemoporoplasticity of calcium leaching in concrete, *Journal of Engineering Mechanics* 125 (10) (1999) 1200–1211.
- [47] F. H. Heukamp, F.-J. Ulm, J. T. Germaine, Poroplastic properties of calcium-leached cement-based materials, *Cement and concrete research* 33 (8) (2003) 1155–1173.
- 680 [48] F.-J. Ulm, G. Constantinides, F. Heukamp, Is concrete a poromechanics materials?—a multiscale investigation of poroelastic properties, *Materials and structures* 37 (1) (2004) 43–58.
- [49] F. Tzschichholz, H. Herrmann, H. Zanni, Reaction-diffusion model for the hydration and setting of cement, *Physical Review E* 53 (3) (1996) 2629.
- 685 [50] E. Stora, B. Bary, Q.-C. He, E. Deville, P. Montarnal, Modelling and simulations of the chemo–mechanical behaviour of leached cement-based materials: leaching process and induced loss of stiffness, *Cement and Concrete Research* 39 (9) (2009) 763–772.
- [51] E. Stora, B. Bary, Q.-C. He, E. Deville, P. Montarnal, Modelling and simulations of the chemo-mechanical behaviour of leached cement-based materials: Interactions between damage and leaching, *Cement and concrete research* 40 (8) (2010) 1226–1236.
- 690 [52] S. A. Silling, Reformulation of elasticity theory for discontinuities and long-range forces, *Journal of the Mechanics and Physics of Solids* 48 (1) (2000) 175–209.



- [53] S. A. Silling, E. Askari, A meshfree method based on the peridynamic model of solid mechanics, *Computers & structures* 83 (17-18) (2005) 1526–1535.
- 695 [54] S. A. Silling, M. Epton, O. Weckner, J. Xu, E. Askari, Peridynamic states and constitutive modeling, *Journal of Elasticity* 88 (2) (2007) 151–184.
- [55] Z. P. Bažant, F.-B. Lin, Non-local yield limit degradation, *International Journal for Numerical Methods in Engineering* 26 (8) (1988) 1805–1823.
- 700 [56] M. Mainguy, C. Tognazzi, J.-M. Torrenti, F. Adenot, Modelling of leaching in pure cement paste and mortar, *Cement and Concrete Research* 30 (1) (2000) 83–90.
- [57] C. Pichler, A. Saxer, R. Lackner, Differential-scheme based dissolution/diffusion model for calcium leaching in cement-based materials accounting for mix design and binder composition, *Cement and concrete research* 42 (5) (2012) 686–699.
- 705 [58] Z. Chen, F. Bobaru, Peridynamic modeling of pitting corrosion damage, *Journal of the Mechanics and Physics of Solids* 78 (2015) 352–381.
- [59] D. De Meo, C. Diyaroglu, N. Zhu, E. Oterkus, M. A. Siddiq, Modelling of stress-corrosion cracking by using peridynamics, *International Journal of Hydrogen Energy* 41 (15) (2016) 6593–6609.
- 710 [60] D. De Meo, E. Oterkus, Finite element implementation of a peridynamic pitting corrosion damage model, *Ocean Engineering* 135 (2017) 76–83.
- [61] D. De Meo, L. Russo, E. Oterkus, Modeling of the onset, propagation, and interaction of multiple cracks generated from corrosion pits by using peridynamics, *Journal of Engineering Materials and Technology* 139 (4) (2017).
- 715 [62] S. Jafarzadeh, Z. Chen, F. Bobaru, Peridynamic modeling of repassivation in pitting corrosion of stainless steel, *Corrosion* 74 (4) (2018) 393–414.
- [63] S. Rokkam, M. Gunzburger, M. Brothers, N. Phan, K. Goel, A nonlocal peridynamics modeling approach for corrosion damage and crack propagation, *Theoretical and Applied Fracture Mechanics* 101 (2019) 373–387.

- [64] P. Demmie, S. Silling, An approach to modeling extreme loading of structures using peridynamics, *Journal of Mechanics of Materials and Structures* 2 (10) (2007) 1921–1945.
- [65] D. Huang, Q. Zhang, P. Qiao, Damage and progressive failure of concrete structures using non-local peridynamic modeling, *Science China Technological Sciences* 54 (3) (2011) 591–596.
- [66] W. Gerstle, N. Sau, S. Silling, Peridynamic modeling of concrete structures, *Nuclear engineering and design* 237 (12-13) (2007) 1250–1258.
- [67] S. Das, C. Hoffarth, B. Ren, B. Spencer, G. Sant, S. D. Rajan, N. Neithalath, Simulating the fracture of notched mortar beams through extended finite-element method and peridynamics, *Journal of Engineering Mechanics* 145 (7) (2019) 04019049.
- [68] Z. Jingjing, Z. Qing, H. Dan, S. Feng, A peridynamic approach for the simulation of calcium silicate hydrate nanoindentation, *Advances in cement research* 28 (2) (2016) 84–91.
- [69] A. Yaghoobi, M. G. Chorzepa, Fracture analysis of fiber reinforced concrete structures in the micropolar peridynamic analysis framework, *Engineering Fracture Mechanics* 169 (2017) 238–250.
- [70] A. Yaghoobi, M. G. Chorzepa, S. S. Kim, et al., Mesoscale fracture analysis of multiphase cementitious composites using peridynamics, *Materials* 10 (2) (2017) 162.
- [71] D. Yang, W. Dong, X. Liu, S. Yi, X. He, Investigation on mode-I crack propagation in concrete using bond-based peridynamics with a new damage model, *Engineering Fracture Mechanics* 199 (2018) 567–581.
- [72] W. Li, L. Guo, Meso-fracture simulation of cracking process in concrete incorporating three-phase characteristics by peridynamic method, *Construction and Building Materials* 161 (2018) 665–675.
- [73] D. Hou, W. Zhang, P. Wang, H. Ma, Microscale peridynamic simulation of damage process of hydrated cement paste subjected to tension, *Construction and Building Materials* 228 (2019) 117053.
- [74] M. Geers, R. De Borst, R. Peerlings, Damage and crack modeling in single-edge and double-edge notched concrete beams, *Engineering Fracture Mechanics* 65 (2-3) (2000) 247–261.

- [75] D. Z. Turner, A non-local model for fluid-structure interaction with applications in hydraulic fracturing, *International Journal for Computational Methods in Engineering Science and Mechanics* 14 (5) (2013) 391–400.
- [76] A. Katiyar, J. T. Foster, H. Ouchi, M. M. Sharma, A peridynamic formulation of pressure driven convective fluid transport in porous media, *Journal of Computational Physics* 261 (2014) 209–229.
- [77] H. Ouchi, A. Katiyar, J. Foster, M. M. Sharma, et al., A peridynamics model for the propagation of hydraulic fractures in heterogeneous, naturally fractured reservoirs, in: *SPE Hydraulic Fracturing Technology Conference*, Society of Petroleum Engineers, 2015.
- [78] H. Ouchi, A. Katiyar, J. York, J. T. Foster, M. M. Sharma, A fully coupled porous flow and geomechanics model for fluid driven cracks: a peridynamics approach, *Computational Mechanics* 55 (3) (2015) 561–576.
- [79] W. Li, L. Guo, A mechanical-diffusive peridynamics coupling model for meso-scale simulation of chloride penetration in concrete under loadings, *Construction and Building Materials* 241 (2020) 118021.
- [80] Y. Xi, Z. P. Bažant, Modeling chloride penetration in saturated concrete, *Journal of Materials in Civil Engineering* 11 (1) (1999) 58–65.
- [81] Z. Bažant, Size effect in tensile and compression fracture of concrete structures: Computational modeling and design., *AEDIFICATIO Publishers, Fracture Mechanics of Concrete Structures*, 3 (1998) 1905–1922.
- [82] Z. Bažant, J. Planas, Fracture and size effect, *Concrete and Other Quasibrittle Materials* (1998) 383–435.
- [83] C.-J. Haecker, E. Garboczi, J. Bullard, R. Bohn, Z. Sun, S. P. Shah, T. Voigt, Modeling the linear elastic properties of portland cement paste, *Cement and Concrete Research* 35 (10) (2005) 1948–1960.
- [84] F. H. Heukamp, Chemomechanics of calcium leaching of cement-based materials at different scales: The role of ch-dissolution and CSH degradation on strength and durability per-

formance of materials and structures, Ph.D. thesis, Massachusetts Institute of Technology (2003).

- 775 [85] R. N. Swamy, Dynamic poisson's ratio of portland cement paste, mortar and concrete, *Cement and Concrete Research* 1 (5) (1971) 559–583.
- [86] J. Brown, C. Pomeroy, Fracture toughness of cement paste and mortars, *Cement and Concrete Research* 3 (4) (1973) 475–480.
- [87] T. Nishikawa, M. Takatsu, M. Daimon, Fracture behavior of hardened cement paste incorporating mineral additions, *Cement and concrete research* 25 (6) (1995) 1218–1224.
- 780 [88] W. Wang, T. Tong, Q. Yu, Subcritical crack growth induced by stress corrosion in hardened cement paste, in: V. Saouma, J. Bolander, E. Landis (Eds.), 9th International Conference on Fracture Mechanics of Concrete and Concrete Structures, 2016, pp. 1–6.
- [89] T. Naik, S. Singh, A. Hassaballah, Effects of water to cementitious ratio on compressive strength of cement mortar containing fly ash, in: *Proceedings of the fourth international conference on fly ash, Silica fume, slag, and natural Pozzolans in concrete*, Istanbul, Turkey, 1992.
- 785 [90] H. Choi, D. Kang, G. S. Seo, W. Chung, Effect of some parameters on the compressive strength of mwent-cement composites, *Advances in Materials Science and Engineering* 2015 (2015).
- 790 [91] J. Su, J.-y. Ye, Z. Fang, M.-h. Zhao, Size effect on cubic and prismatic compressive strength of cement paste, *Journal of Central South University* 22 (10) (2015) 4090–4096.
- [92] K. Pimenta Teixeira, I. Perdigão Rocha, L. De Sá Carneiro, J. Flores, E. A. Dauer, A. Ghahremaninezhad, The effect of curing temperature on the properties of cement pastes modified with tio2 nanoparticles, *Materials* 9 (11) (2016) 952.
- 795 [93] M. Zhang, G. Ye, K. Van Breugel, Microstructure-based modeling of water diffusivity in cement paste, *Construction and Building Materials* 25 (4) (2011) 2046–2052.
- [94] F. Adenot, M. Buil, Modelling of the corrosion of the cement paste by deionized water, *Cement and Concrete research* 22 (2-3) (1992) 489–496.

- [95] A. Delagrave, J. Marchand, E. Samson, Prediction of diffusion coefficients in cement-based materials on the basis of migration experiments, *Cement and Concrete Research* 26 (12) (1996) 1831–1842.
- [96] M. E. Tadros, J. Skalny, R. S. Kalyoncu, Kinetics of calcium hydroxide crystal growth from solution, *Journal of Colloid and Interface Science* 55 (1) (1976) 20–24.
- [97] J. W. Bullard, E. Enjolras, W. L. George, S. G. Satterfield, J. E. Terrill, A parallel reaction-transport model applied to cement hydration and microstructure development, *Modelling and Simulation in Materials Science and Engineering* 18 (2) (2010) 025007.
- [98] R. F. Feldman, Diffusion measurements in cement paste by water replacement using propan-2-ol, *Cement and Concrete Research* 17 (4) (1987) 602–612.
- [99] W. P. Halperin, J.-Y. Jehng, Y.-Q. Song, Application of spin-spin relaxation to measurement of surface area and pore size distributions in a hydrating cement paste, *Magnetic Resonance Imaging* 12 (2) (1994) 169–173.
- [100] X. Wang, K. Xu, Y. Li, S. Guo, Dissolution and leaching mechanisms of calcium ions in cement based materials, *Construction and Building Materials* 180 (2018) 103–108.
- [101] K. H. Khayat, Viscosity-enhancing admixtures for cement-based materials—an overview, *Cement and Concrete Composites* 20 (2-3) (1998) 171–188.
- [102] O. Coussy, P. Dangla, T. Lassabatère, V. Baroghel-Bouny, The equivalent pore pressure and the swelling and shrinkage of cement-based materials, *Materials and structures* 37 (1) (2004) 15–20.
- [103] G. Giaccio, R. Zerbino, J. Ponce, O. R. Batic, Mechanical behavior of concretes damaged by alkali-silica reaction, *Cement and Concrete Research* 38 (7) (2008) 993–1004.
- [104] U. Berner, Modelling the incongruent dissolution of hydrated cement minerals, *Radiochimica Acta* 44 (2) (1988) 387–394.
- [105] R. Feldman, P. Sereda, A new model for hydrated portland cement and its practical implications, *Engineering Journal* 53 (8-9) (1970) 53–59.

- [106] S. Goñi, M. Lorenzo, A. Guerrero, M. Hernández, Calcium hydroxide saturation factors in the pore solution of hydrated portland cement fly ash pastes, *Journal of the American Ceramic Society* 79 (4) (1996).
- [107] O. M. Jensen, P. F. Hansen, Water-entrained cement-based materials: I. principles and theoretical background, *Cement and concrete research* 31 (4) (2001) 647–654.
- [108] D. Anstice, C. Page, M. Page, The pore solution phase of carbonated cement pastes, *Cement and Concrete Research* 35 (2) (2005) 377–383.
- [109] A. Bede, A. Scurtu, I. Ardelean, Nmr relaxation of molecules confined inside the cement paste pores under partially saturated conditions, *Cement and Concrete Research* 89 (2016) 56–62.
- [110] P. Lura, F. Winnefeld, X. Fang, A simple method for determining the total amount of physically and chemically bound water of different cements, *Journal of Thermal Analysis and Calorimetry* 130 (2) (2017) 653–660.
- [111] A. Atkinson, A. Nickerson, The diffusion of ions through water-saturated cement, *Journal of materials science* 19 (9) (1984) 3068–3078.
- [112] R. R. Lloyd, J. L. Provis, J. S. Van Deventer, Pore solution composition and alkali diffusion in inorganic polymer cement, *Cement and Concrete Research* 40 (9) (2010) 1386–1392.
- [113] U. Berner, Evolution of pore water chemistry during degradation of cement in a radioactive waste repository environment, *Waste management* 12 (2-3) (1992) 201–219.
- [114] S. Mindess, F. Young, D. Darwin, *Concrete*, Prentice-Hall, 1981.
- [115] S. H. Kosmatka, B. Kerkhoff, W. C. Panarese, et al., *Design and control of concrete mixtures*, Vol. 5420, Portland Cement Association Skokie, IL, 2002.
- [116] M. S. Mamlouk, J. P. Zaniewski, *Materials for civil and construction engineers*, Pearson Prentice Hall Upper Saddle River, NJ, 2006.
- [117] S. Swanton, T. Heath, A. Clacher, Leaching behaviour of low Ca:Si ratio  $\text{CaO-SiO}_2\text{-H}_2\text{O}$  systems, *Cement and Concrete Research* 88 (2016) 82–95.

- [118] V. Nguyen, H. Colina, J. M. Torrenti, C. Boulay, B. Nedjar, Chemo-mechanical coupling behaviour of leached concrete: Part i: Experimental results, *Nuclear Engineering and Design* 237 (20-21) (2007) 2083–2089.
- [119] C. Le Bellégo, J. F. Dubé, G. Pijaudier-Cabot, B. Gérard, Calibration of nonlocal damage model from size effect tests, *European Journal of Mechanics-A/Solids* 22 (1) (2003) 33–46.
- [120] E. Stora, Q.-C. He, B. Bary, A mixed composite spheres assemblage model for the transport properties of random heterogeneous materials with high contrasts, *Journal of applied physics* 100 (8) (2006) 084910.
- [121] P. Chindaprasirt, C. Jaturapitakkul, T. Sinsiri, Effect of fly ash fineness on compressive strength and pore size of blended cement paste, *Cement and Concrete Composites* 27 (4) (2005) 425–428.
- [122] J. J. Thomas, J. J. Chen, A. J. Allen, H. M. Jennings, Effects of decalcification on the microstructure and surface area of cement and tricalcium silicate pastes, *Cement and Concrete Research* 34 (12) (2004) 2297–2307.
- [123] T. L. Anderson, *Fracture mechanics: fundamentals and applications*, CRC press, 2017.
- [124] E. T. Jaynes, Information theory and statistical mechanics, *Physical review* 106 (4) (1957) 620.
- [125] E. T. Jaynes, Information theory and statistical mechanics. II, *Physical review* 108 (2) (1957) 171.
- [126] I. M. Sobol, Global sensitivity indices for nonlinear mathematical models and their monte carlo estimates, *Mathematics and computers in simulation* 55 (1-3) (2001) 271–280.
- [127] A. Saltelli, M. Ratto, T. Andres, F. Campolongo, J. Cariboni, D. Gatelli, M. Saisana, S. Tarantola, *Global sensitivity analysis: the primer*, John Wiley & Sons, 2008.
- [128] V. Eglajs, P. Audze, New approach to the design of multifactor experiments, *Problems of Dynamics and Strengths* 35 (1) (1977) 104–107.

- [129] M. D. McKay, R. J. Beckman, W. J. Conover, A comparison of three methods for selecting values of input variables in the analysis of output from a computer code, *Technometrics* 42 (1) (2000) 55–61.
- [130] A. Gholizadeh-Vayghan, F. Rajabipour, Quantifying the swelling properties of alkali-silica reaction (ASR) gels as a function of their composition, *Journal of the American Ceramic Society* 100 (8) (2017) 3801–3818.
- [131] W. Vichit-Vadakan, G. W. Scherer, Measuring permeability and stress relaxation of young cement paste by beam bending, *Cement and concrete research* 33 (12) (2003) 1925–1932.
- [132] J. A. Mitchell, A non-local, ordinary-state-based viscoelasticity model for peridynamics, *Sandia National Lab Report* 8064 (2011) 1–28.
- [133] O. Weckner, N. A. N. Mohamed, Viscoelastic material models in peridynamics, *Applied Mathematics and Computation* 219 (11) (2013) 6039–6043.
- [134] S. Nadimi, I. Miscovic, J. McLennan, A 3d peridynamic simulation of hydraulic fracture process in a heterogeneous medium, *Journal of Petroleum Science and Engineering* 145 (2016) 444–452.
- [135] E. Samson, J. Marchand, Modeling the effect of temperature on ionic transport in cementitious materials, *Cement and Concrete Research* 37 (3) (2007) 455–468.
- [136] L. Charpin, Y. Le Pape, É. Coustabeau, É. Toppani, G. Heinfling, C. Le Bellego, B. Masson, J. Montalvo, A. Courtois, J. Sanahuja, et al., A 12 year edf study of concrete creep under uniaxial and biaxial loading, *Cement and Concrete Research* 103 (2018) 140–159.
- [137] R. E. Jones, J. A. Zimmerman, The construction and application of an atomistic j-integral via hardy estimates of continuum fields, *Journal of the Mechanics and Physics of Solids* 58 (9) (2010) 1318–1337.
- [138] J. A. Zimmerman, D. J. Bammann, H. Gao, Deformation gradients for continuum mechanical analysis of atomistic simulations, *International Journal of Solids and Structures* 46 (2) (2009) 238–253.



- [139] R. Jabakhanji, R. H. Mohtar, A peridynamic model of flow in porous media, *Advances in water resources* 78 (2015) 22–35.
- [140] C. Cattaneo, A form of heat-conduction equations which eliminates the paradox of instantaneous propagation, *Comptes Rendus* 247 (1958) 431.
- [141] J. Bonet, R. D. Wood, *Nonlinear continuum mechanics for finite element analysis*, Cambridge university press, 1997.
- [142] R. E. Jones, P. Papadopoulos, A yield-limited lagrange multiplier formulation for frictional contact, *International Journal for Numerical Methods in Engineering* 48 (8) (2000) 1127–1149.

## 6. Appendix: Method details

In this appendix we provide the theoretical and computational details on our implementation of the peridynamics (PD) method. We begin with the fundamental premise of PD as a kernel-based reformulation of the continuum mechanics. We cover both the formulation for mechanical deformation and chemical transport given in Sec. 2, and the coupled scheme for solution of the evolution of the displacement and concentration fields. We provide details on how we calibrate the kernel size and use dynamic boundary conditions to simulate fluid infiltration into fractures. Connections to the constitutive behavior outlined in Sec. 2, given in detail in this section, are summarized in Sec. 3.

### A.1. Mechanical

In the (bond-based) PD framework the momentum balance, Eq. (1), takes the form

$$\mathbf{0} = \underbrace{\int_{\Omega} \mathbf{f}(\mathbf{u}' - \mathbf{u}, \mathbf{X}' - \mathbf{X}) \omega(\mathbf{X}' - \mathbf{X}) dV'}_{\mathbf{R}^u} \quad (\text{A.29})$$

where  $\mathbf{f}$  is the force (density) kernel,  $\omega$  is the localization function, and  $\mathbf{R}^u$  is the displacement residual formed from the right hand side of this governing equation. Note that we have omitted the body force  $\rho \mathbf{b}$  for simplicity at this stage. We define  $\boldsymbol{\eta} \equiv \mathbf{u}' - \mathbf{u}$  as the difference in displacements between the point of interest  $\mathbf{X}$  and a neighboring point  $\mathbf{X}'$  in the reference configuration, and

likewise  $\Xi \equiv \mathbf{X}' - \mathbf{X}$  as the difference in reference positions. For this work, we use a uniform top-hat localization

$$\omega(\mathbf{X}' - \mathbf{X}) = \begin{cases} \frac{1}{V_h} & \text{for } \mathbf{X} \in B_h(\mathbf{X}) \\ 0 & \text{else} \end{cases} \quad (\text{A.30})$$

normalized so that

$$\int_{\Omega} \omega(\mathbf{X}' - \mathbf{X}) dV' = 1 \quad (\text{A.31})$$

for  $B_h \subset \Omega$ . Hence, the integration domain for Eq. (A.29) can be changed to the ball  $B_h(\mathbf{X})$  of radius  $h$  around any point of interest  $\mathbf{X}$

$$\mathbf{0} = \frac{1}{V_h} \int_{B_h(\mathbf{X})} \mathbf{f}(\mathbf{u}' - \mathbf{u}, \mathbf{X}' - \mathbf{X}) dV' \quad (\text{A.32})$$

920 where  $V_h = \pi h^2$  is the volume of the 2D ball. The force kernel  $\mathbf{f}$  is dimensionally force per volume (a force density).

The method is made discrete after the introduction of representative particles (indexed by  $I$ )

$$\mathbf{0} \approx \underbrace{\frac{1}{V_h} \sum_{\mathbf{X}_J \in B_h(\mathbf{X})} \mathbf{f}(\mathbf{u}_J - \mathbf{u}_I, \mathbf{X}_J - \mathbf{X}_I) \Delta V_J}_{\mathbf{R}_I^u} \quad (\text{A.33})$$

We take all the quadrature weights  $\Delta V_J = \Delta V$  to be the same and tune the horizon  $h$  to minimize quadrature error. We construct the point cloud defining the domain on a lattice, in this case a 2D close packed lattice with 2 particles per unit cell. We set  $\Delta V = s^2/2$  where  $s$  is the side length of the square unit cell so that the quadrature preserves volume. As in Ref. [137], the quadrature error for the localization alone is proportional to

$$\frac{V}{V_h} = \frac{1}{\pi h^2} \sum_{\mathbf{X}_J \in B_h(\mathbf{X})} \Delta V_J = \frac{N \Delta V}{\pi h^2}, \quad (\text{A.34})$$

where  $V$  is the volume  $B_h$  estimated by quadrature and  $V_h$  is its precise volume. So choosing  $h$  such that  $\pi h^2 = N \Delta V$  minimizes this error where  $N$  is the number of points in  $B_h(\mathbf{X})$ . This error can be interpreted as the zeroth order quadrature error for a nearly constant force kernel where  
 925 the horizon  $h$  is small relative to the scale of the change in the kinematic field. Fig. 19 shows the relative error  $(V - V_h)/V_h$  for a 2D close packed lattice of points as a function of the horizon  $h$  relative to the (square) unit cell size  $s$ . Numerous roots of the error are given in Table 4.

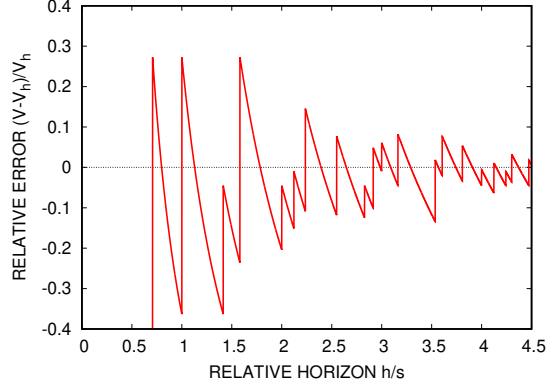


Figure 19: Quadrature error  $(V - V_h)/V_h$  versus horizon  $h$  relative to the (square) unit cell size  $s$ .

$N$	4	8	20	36	44	56	60	68	80	88	96	108	120
$h/s$	0.797	1.128	1.784	2.393	2.646	2.985	3.090	3.289	3.568	3.742	3.908	4.145	4.370

Table 4: Optimal relative horizon  $h/s$  and number of neighboring points  $N$  for a 2D close packed lattice of points.

Since the force density:

$$\mathbf{r}(\mathbf{X}) = \frac{1}{V_h} \int_{B_h(\mathbf{X})} \mathbf{f}(\mathbf{u}' - \mathbf{u}, \mathbf{X}' - \mathbf{X}) dV' , \quad (\text{A.35})$$

is an analog to  $\nabla \cdot \mathbf{P}$ , refer to Eq. (1), the reaction force on region  $R$  can be obtained from

$$\begin{aligned} \mathbf{R}_R &= \int_R \mathbf{r}(\mathbf{X}) dV \\ &\approx \sum_{\mathbf{X}_I \in R} \mathbf{r}(\mathbf{X}_I) \Delta V_I = \frac{1}{V_h} \sum_{\mathbf{X}_I \in R} \sum_{\mathbf{X}_J \in B_h(\mathbf{X})} \mathbf{f}(\mathbf{u}_J - \mathbf{u}_I, \mathbf{X}_J - \mathbf{X}_I) \Delta V_J \Delta V_I \end{aligned} \quad (\text{A.36})$$

We can also recover the (non-local) deformation gradient [138] at any node  $I$  via

$$\mathbf{F}_I = \left[ \sum_{\mathbf{X}_J \in B_h(\mathbf{X})} \mathbf{x}_J \otimes \mathbf{X}_J \Delta V_J \right] \left[ \sum_{\mathbf{X}_J \in B_h(\mathbf{X})} \mathbf{X}_J \otimes \mathbf{X}_J \Delta V_J \right]^{-1} \quad (\text{A.37})$$

where  $J$  runs through the set of neighbors within the horizon  $h$  around  $\mathbf{X}_I$ .

Now turning to the specific form of  $\mathbf{f}$ , the mechanical constitutive model for a brittle material is typically [53]

$$\mathbf{f} = f(\lambda) \mu \frac{\boldsymbol{\xi}}{\|\boldsymbol{\xi}\|} . \quad (\text{A.38})$$

The magnitude of the force density  $f$  is simply

$$f(\lambda) = k\lambda , \quad (\text{A.39})$$

where  $k$  is a particle-particle bond stiffness, and the bond stretch  $\lambda$  is

$$\lambda = \frac{\|\boldsymbol{\xi}\| - \|\boldsymbol{\Xi}\|}{\|\boldsymbol{\Xi}\|} \quad (\text{A.40})$$

where recall  $\boldsymbol{\xi} \equiv \mathbf{x}' - \mathbf{x}$  and  $\boldsymbol{\Xi} \equiv \mathbf{X}' - \mathbf{X}$ . This linear relation is subject to tensile and compressive  
930 limits. Tensile failure ( $\lambda > \lambda_{\max}$ ) is associated with decohesion/fracture, while the compressive  
limit ( $\lambda < \lambda_{\min}$ ) models void collapse and subsequent stress concentrations. Both limits result in  
abrupt breakage for this classical bond function. The state variable  $\mu$  accounts for the irreversibility  
of breakage in that it is equal to one if  $\lambda_{\min} < \lambda < \lambda_{\max}$ , for all time up to the present (the bond is  
intact) and zero otherwise (the bond has been broken). As mentioned, this is the standard (bond-  
935 based) PD mechanical model with basic parameters: stiffness  $k$ , and strengths  $\lambda_{\min}$  and  $\lambda_{\max}$ . It  
is effectively a central force potential and results in a brittle elastic material with Poisson's ratio  
equal to 1/4.

The stiffness parameter  $k$  can be related to bulk modulus  $B$  by equating the elastic energy  
between a linear elastic material and its PD analog for an isotropic plane strain expansion in 2D  
 $\lambda = \epsilon \|\boldsymbol{\Xi}\|$ :

$$k = \frac{12B}{h} \propto \frac{B}{h} \propto \frac{E}{h} . \quad (\text{A.41})$$

The tensile limit  $\lambda_{\max}$  can be related to the fracture toughness  $K_{Ic}$  via

$$\lambda_{\max} = K_{Ic} \sqrt{\frac{\pi}{3E^*Bh}} \propto \frac{K_{Ic}}{E\sqrt{h}} , \quad (\text{A.42})$$

which is based on the cohesive energy of a region  $B_h$  split into hemispheres, which we have special-  
ized to 2D following Ref. [53]. Here,  $E^* = 1/(1 - \nu^2)$  is the appropriate mode I elastic modulus for  
plane strain. The compressive limit  $\lambda_{\min}$  is more problematical since it is related to void collapse  
and related processes. Nevertheless, we expect

$$\lambda_{\min} \propto \frac{\sigma_c}{E} , \quad (\text{A.43})$$

where  $\sigma_c$  is a measured compressive strength.

We also allow for shrinkage via a change in the reference configuration volume. We adjust the  
definition of stretch Eq. (A.40) to accommodate this:

$$\lambda = \frac{\|\boldsymbol{\xi}\| - (1 + \alpha)\|\boldsymbol{\Xi}_0\|}{(1 + \alpha)\|\boldsymbol{\Xi}_0\|} \quad (\text{A.44})$$

where  $\Xi_0$  is the difference in reference positions for a pristine material and  $\alpha$  is the radial shrinkage strain introduced earlier.

### A.2. Transport

PD is primarily applied in the mechanical regime to simulate fracture processes, but it can also be applied to transport, where the analog to Eq. (2) is

$$\dot{c} = \underbrace{\int_{\Omega} j(c' - c, \mathbf{x}' - \mathbf{x}) \omega(\mathbf{X}' - \mathbf{X}) dV'}_{\mathbf{R}^c} + r \quad (\text{A.45})$$

and, recall,  $c = c(\mathbf{x}, t)$  and  $c' = c(\mathbf{x}', t)$  are lists of mobile species which, in our development, is limited to water  $\tilde{c}$ . Here  $\mathbf{R}^c$  is the concentration residual formed from the right hand side of this governing equation. For simplicity, we use the same localization  $\omega$ , horizon  $h$ , and point cloud for discretization for chemical transport as for the mechanical aspects of the problem.

The constitutive model [139, 79] for diffusion employs the kernel

$$j(\zeta) = \kappa \frac{\zeta}{\|\boldsymbol{\xi}\|} , \quad (\text{A.46})$$

where  $\zeta = c - c'$  is a difference in concentration at  $\mathbf{x}$  and  $\mathbf{x}'$ . (Note this kernel is defined in the current configuration of the material.) As with  $f$  in Eq. (A.39),  $j$  is linear in its primary argument and  $\kappa$  is a bond diffusion parameter. Here, we omit  $\mu$ , the bond state variable, since we expect more flow in damaged/degraded regions and open fractures and adjust  $\kappa$  (due to degradation) or  $c$  (due to fracture) accordingly (see Sec. A.3).

By equating the power dissipated for a uniform flow with the ball  $B_h$ , the PD parameter  $\kappa$  can be related to the continuum diffusion constant  $D$  [139]

$$\kappa = \frac{6D}{h} \propto \frac{D}{h} \quad (\text{A.47})$$

The reaction model, like the body force in Eq. (1), seems to be able to be used without translation; however, we found we needed to correct for the infinite speed of propagation of the diffusion front in order to preserve a sharp reaction front [19, 20, 17]. To effect the step-like reaction front seen in Haga *et al.* [19] Fig. 7, we employ a step-like function  $v$  in Eq. (11)

$$\dot{c} = -Kv(\tilde{c})\tilde{c} \quad (\text{A.48})$$

to start the reaction only after sufficient water is present. At first we used a soft step based on the logistic function, but in order to have the reaction front be less than  $\approx 1$  cm from the diffusion front this function needed to be so sharp that a true step at threshold, which we arbitrary chose as  $\tilde{c} = 1/2$ , was more efficient. The effects of this treatment on transport and reaction will be demonstrated in  
955 Sec. 4.1.4. (A alternative diffusion with finite speed of propagation, of using the Maxwell-Cattaneo equation [140], was considered but the implementation complexities and wave-like artifacts made the step regularization more attractive.)

### A.3. Boundary conditions

Given the non-local nature of PD, we need to adapt the traditional boundary conditions. To effect Dirichlet boundary conditions such as prescribed displacement, the displacements are penalized in a finite region  $\Gamma$  near the boundary that contains nodes  $\mathbf{X}_I$ . We formulate the penalizations of each boundary condition (indexed by  $a$ ) via potentials  $\phi_a = 1/2 \epsilon g_a(\mathbf{x})^2$  in terms of a constraint (functional)  $g_a(\mathbf{x}) = 0$  and a penalty parameter  $\epsilon \approx 10^3 k$ , where  $k$  is the bond stiffness. The Gâteaux derivative of the potential  $\phi_a$  gives the constraint force density  $\mathbf{f}_a$ :

$$\mathbf{f}_a = \mathbf{D}[\phi_a, \mathbf{x}] = \epsilon g_a(\mathbf{x}) \mathbf{D}[g_a(\mathbf{x}), \mathbf{x}] \quad (\text{A.49})$$

We add the force density  $\mathbf{f}_a$  for each constraint  $g_a$  to the governing equation

$$\mathbf{0} = \int_{B_h(\mathbf{x})} \mathbf{f}(\mathbf{u}' - \mathbf{u}, \mathbf{X}' - \mathbf{X}) \omega(\mathbf{X}' - \mathbf{X}) dV' + \sum_a \int_{\Gamma_a} \mathbf{f}_a(\mathbf{x}') dV' . \quad (\text{A.50})$$

For instance,  $g_a(\mathbf{x}) = \|\mathbf{u}(\mathbf{x}) - \bar{\mathbf{u}}_a\|$ ,

$$\mathbf{f}_a(\mathbf{x}_I) = \epsilon(\mathbf{u}_I - \bar{\mathbf{u}}_a) . \quad (\text{A.51})$$

where  $\bar{\mathbf{u}}_a$  is a prescribed function and  $\mathbf{x}_I$  is the position of any particle  $I$  in the constraint group. Here we have used the Gâteaux derivative [141] of the magnitude of a vector

$$\mathbf{D}[\|\mathbf{y}\|, \mathbf{u}] = \frac{\mathbf{y}}{\|\mathbf{y}\|} \mathbf{D}[\mathbf{y}, \mathbf{u}] . \quad (\text{A.52})$$

The Gâteaux derivative of a unit vector [141]

$$\mathbf{D}\left[\frac{\mathbf{y}}{\|\mathbf{y}\|}, \mathbf{u}\right] = \frac{1}{\|\mathbf{y}\|} \left( \mathbf{I} - \frac{\mathbf{y}}{\|\mathbf{y}\|} \otimes \frac{\mathbf{y}}{\|\mathbf{y}\|} \right) \mathbf{D}[\mathbf{y}, \mathbf{u}] \quad (\text{A.53})$$

is also useful in formulating the constraint force

$$\mathbf{f}_a(\mathbf{x}_I) = \epsilon(\mathbf{u}_I - \bar{\mathbf{u}}_a) \cdot \mathbf{n}_a \mathbf{n}_a \quad (\text{A.54})$$

in a given direction  $\mathbf{n}_a$  normal to the unconstrained direction for a roller/slider constraint  $g_a(\mathbf{x}) = (\mathbf{u}(\mathbf{x}) - \bar{\mathbf{u}}_a) \cdot \mathbf{n}_a$ . A pin which allows rotation can be described by  $g_a(\mathbf{x}_I) = \|\mathbf{x}_I - \bar{\mathbf{x}}_a\| - L_I$ , and has an associated force

$$\mathbf{f}_a(\mathbf{x}_I) = \epsilon(\|\mathbf{x}_I - \bar{\mathbf{x}}_a\| - L_I) \frac{(\mathbf{x}_I - \bar{\mathbf{x}}_a)}{\|\mathbf{x}_I - \bar{\mathbf{x}}_a\|} \quad (\text{A.55})$$

where  $\bar{\mathbf{x}}_a(t)$  is prescribed and  $L_I \equiv \|\mathbf{X}_I - \bar{\mathbf{x}}_a\|$ . A pin on a slider uses the pin constraint  $g_a(\mathbf{x}_I) = \|\mathbf{x}_I - \bar{\mathbf{x}}_a\| - L_I$ , and an auxiliary equation  $\mathbf{f}_a \cdot \mathbf{n}_a = 0$  which determines the component of  $\bar{\mathbf{x}}_a$  perpendicular to  $\mathbf{n}_a$ .

One of the advantages of penalization of the boundary conditions is that they can be applied dynamically without altering the methods used to form Eq. (A.29). We use this to effect adaptive concentration boundary conditions on the water concentration  $\underline{c}$  to emulate fluid infiltration in newly formed fractures. In our applications, fracture and infiltration occur on much shorter timescales than diffusion, so that we can treat them as happening instantaneously. Hence, where fracture occurs we apply the Dirichlet condition  $\tilde{c} = \tilde{c}_\infty$ , where  $\tilde{c}_\infty \equiv 1$  is the bulk water concentration, on the nodes of the newly formed surfaces. These points are identified by having half of their bonds broken. Although based on the local separation of the domain along a flat surface, this is a somewhat arbitrary threshold. As will be shown in Sec. 4, this criterion produces physically plausible results.

#### A.4. Displacement solve and concentration update

The PD balance of linear momentum Eq. (A.29) is a system of nonlinear equations which we solve with a Newton-Raphson method. The linearization of the force density kernel  $\mathbf{f}$ , Eq. (A.38) is

$$\mathbf{L}[\mathbf{f}, \mathbf{u}]|_{\mathbf{u}=\mathbf{0}} = \mathbf{f}|_{\mathbf{u}=\mathbf{0}} + \mathbf{D}[\mathbf{f}, \mathbf{u}]|_{\mathbf{u}=\mathbf{0}} \cdot \Delta \mathbf{u} = \mathbf{0} \quad (\text{A.56})$$

where

$$\mathbf{D}[\mathbf{f}, \mathbf{u}] = \left( \frac{F'}{\xi} [\boldsymbol{\xi} \otimes \boldsymbol{\xi}] + f \mathbf{I} \right) \mathbf{D}[\boldsymbol{\xi}, \mathbf{u}] \quad (\text{A.57})$$

since  $\mathbf{D}[\boldsymbol{\xi}, \boldsymbol{\xi}] = \frac{1}{\xi} \boldsymbol{\xi}$ ,  $F(\xi) = f(\xi)/\xi$ ,  $\xi = \|\boldsymbol{\xi}\|$ , and  $\boldsymbol{\xi} = \mathbf{u}' - \mathbf{u} + \mathbf{X}' - \mathbf{X}$ . For  $F(\xi) = k \frac{\xi - L}{\xi L}$ ,

$$F'(\xi) = k \left( \frac{1}{\xi L} - \frac{\xi - L}{\xi^2 L} \right) = \frac{k}{\xi^2}, \quad (\text{A.58})$$

where  $k$  is the bond stiffness.

Bond breakage induces non-smoothness that frustrates the convergence of the Newton-Raphson method. We considered regularizing failure with soft breakage of bonds by adding linear decay with

negative slope,  $10k$ , as in cohesive zone and atomic bond models. However, controlling the active set by updating bond states  $\mu$  on schedule where  $\lambda_{\min}$  and  $\lambda_{\max}$  are inflated and then reduced in stages during the displacement solve so most stretched bond fail first, as in [142], performed better, was more stable, and incurred fewer artifacts in the response.

To integrate the coupled dynamic transport, Eq. (A.45), and quasi-static mechanical governing equations, Eq. (A.29), we employed a nested fractional step approach based on the explicit midpoint with subcycling since the displacement solve is expensive. The scheme has three basic steps:

$$m \text{ transport steps } c_{n+i+1} = c_{n+i} + \frac{1}{2}\Delta t \mathbf{R}^c(\mathbf{u}_{n-m}, c_{n+i}), \quad i = 0..m-1 \quad (\text{A.59})$$

$$\text{displacement solve} \quad \mathbf{0} = \mathbf{R}^u(\mathbf{u}_{n+m}, c_{n+m}) \quad (\text{A.60})$$

$$m \text{ transport steps } c_{n+i+1} = c_{n+i} + \frac{1}{2}\Delta t \mathbf{R}^c(\mathbf{u}_{n+m}, c_{n+i}), \quad i = m..2m-1 \quad (\text{A.61})$$

980 where the subscripts refer to discrete times and indexing across nodes is implicit. The residuals  $\mathbf{R}^u$  and  $\mathbf{R}^c$  are defined in Eq. (A.29) and Eq. (A.45), respectively.